Data-driven failure criteria prediction in composite wing boxes using machine learning

Original
Data-driven failure criteria prediction in composite wing boxes using machine learning / Magliacano, D., Tufano, V., Letizia, A., Sessa, B., Filippi, M.. - In: COMPOSITE STRUCTURES. - ISSN 0263-8223. - ELETTRONICO. - 373:(2025). [10.1016/j.compstruct.2025.119675]

Publisher:
Elsevier

Published
DOI:10.1016/j.compstruct.2025.119675

Composite Structures 373 (2025) 119675

Contents lists available at ScienceDirect

Composite Structures

journal homepage: www.elsevier.com/locate/compstruct

Data-driven failure criteria prediction in composite wing boxes using machine learning

Dario Magliacano [a],*, Vincenza Tufano [b], Annalisa Letizia [b], Bernardo Sessa [b], Matteo Filippi [a]

[a] *Department of Mechanical and Aerospace Engineering, Politecnico di Torino, Corso Duca degli Abruzzi 24, Turin, 10129, TO, Italy*
[b] *Teoresi S.p.A., Via Perugia 24, Turin, 10152, TO, Italy*

ARTICLE INFO

Keywords:
Data-driven
Machine learning
Structural health prediction
Composite
Material properties
Wing box

ABSTRACT

Modern transport aircraft exploit composite wing-box architectures to maximize strength-to-weight efficiency, yet the through-thickness damage states that govern air-worthiness remain difficult to quantify by closed-form analysis. A fully labeled benchmark data set, comprising 1017 finite-element (FE) simulations of a Cirrus-class carbon-fiber wing-box (nine undamaged cases plus 1008 damage scenarios obtained by combining 28 intralaminar damage locations with four severity levels for each of nine orthotropic materials) is therefore generated. Five classical failure criteria (Max-Stress, Tsai–Wu, Tsai–Hill, Hashin and Christensen) are evaluated at the most-stressed element and adopted as supervised-learning targets. Two regression surrogates, Random Forest (RF) ensembles and Support Vector Regression (SVR), are trained on the material-property vector and damage descriptors. A material-wise leave-one-out (LOO) cross-validation strategy demonstrates that the RF model attains a root-mean-square error RMSE = 0.076 for the Hashin index, while preserving RMSE $\leq$ 0.15 on the Max-Stress index. The resulting RF surrogate furnishes near-instant predictions of composite failure indices and provides a reliable machine-learning benchmark for operational wing-box health assessment.

1. Introduction

In the past decade composite-structure health assessment has progressed from global vibration signatures to high-fidelity, data-driven surrogates capable of regressing or classifying multi-axial failure states with aircraft-grade reliability, as summarized in Table 1, where: σ_a is the stress amplitude (half the range of the cyclic axial stress); V_f is the fiber-volume fraction (volume of fiber divided by volume of composite); t is the Coupon (laminate) thickness; and N_f is the number of cycles to failure. Early surveys noted the promise of artificial-intelligence techniques for damage detection but still relied on handcrafted frequency or wavelet features [1,2]. More recent contributions harness full-field strain maps, acoustic-emission spectra or synthesis-based finite-element (FE) databases to train ensemble learners that achieve coefficients of determination R^2 above 0.90 for matrix-cracking thresholds or residual tensile strength [3]. Support vector machines with classical and quantum kernels have delivered classification accuracies beyond 90% for open-hole laminate failure envelopes, illustrating the benefit of kernel alignment in small-sample regimes [4]. Gradient-boosting decision trees further reduce the root-mean-square error in multi-factor fatigue-life prediction by up to 35% compared with support-vector regression, while preserving physical monotonicity trends [3]. Deep transfer-learning frameworks now localize delamination and quantify severity directly from limited Lamb-wave or thermo-graphic imagery, thereby eliminating exhaustive manual feature engineering [5].

Despite these advances, integrated composite wing-box assemblies remain under-represented. The present study fills this gap by training a supervised-learning surrogate on FE realizations that span the material-property envelope of modern transport-category aircraft, benchmarking random forests against support-vector regression models, and validating the surrogate against FE solutions.

The literature review on structural health prediction and the application of machine learning algorithms in Structural Health Monitoring (SHM) constitute the next sub-sections. Afterwards, Section 2 describes the methodological framework of the current research regarding data acquisition, preprocessing, and the development of the machine learning architecture. Section 3 deals with the presentation and discussion of results with a view to assessing the performance evaluation metrics and predictive efficiency of the ML model. Finally, Section 4 concludes the paper.

1.1. Background and motivation

The high strength-to-weight ratio of composite wing boxes has revolutionized conventional design in modern aircraft and eventually

---

* Corresponding author.
E-mail address: dario.magliacano@polito.it (D. Magliacano).

https://doi.org/10.1016/j.compstruct.2025.119675
Received 11 April 2025; Received in revised form 28 August 2025; Accepted 16 September 2025

Table 1
Representative machine-learning studies on composite-structure failure or damage prognosis (2024–2025).

Author (Year)	Structure	Inputs	Targets	Model | Accuracy
Spencer et al. (2025) [1]	Generic FRP beams	Vibration spectra	Binary damage flag	CNN | F1 = 0.92
Numan (2024) [2]	CFRP plates	Accel. features	Damage class	SVM | F1 = 0.88
Aydın & Cakiroglu (2025) [3]	Wind-blade coupon	σ_a, V_f, t	$\log N_f$	XGBoost | RMSE = 0.31
Tosti Balducci et al. (2024) [4]	Open-hole laminate	In-plane loads	Safe/fail label	SVM (RBF) | Acc. = 0.94
Azad et al. (2024) [5]	CFRP panel	Lamb-wave set	Location & depth	ResNet | MAE = 6 mm
Karuppusamy et al. (2025) [6]	Review	–	–	–

provides better fuel efficiency and higher performance. Composites find a central place in modern aircraft design because these materials demonstrate very good strength-to-weight ratio compared to the traditional metal counterparts. This advantage translates into several key benefits for aircraft performance.

The reduction in weight of composite wing boxes leads to a reduction in fuel consumption, opening up many possibilities by increasing the range or payload. In addition, the aerodynamic efficiency is improved by streamlined design and smooth surfaces, which further reduce fuel consumption and possibly permit higher aircraft speeds. Composites provide a greater range of design options than metals, allowing for complex wing shapes to be constructed to maximize aerodynamics and push the boundaries of aircraft design.

While composite wing boxes have several advantages, their very nature introduces variability. While composite wing boxes have several advantages, their very nature introduces variability. Composites are not homogeneous materials; rather, they consist of fibers in a resin matrix, and variability in material properties through the structure influences the heterogeneity of damage-condition characteristics that are important to predicting the health of the wing box, such as the ability to withstand fatigue loads [7,8]. Another factor to be taken into account, which could complicate prediction of health, is the degradation of composite materials stemming from environmental causes, such as moisture action, temperature fluctuation, and ultraviolet radiation.

Reliable methods of prediction of the structural health are required to ensure aircraft safety and schedule maintenance. By examining the limitations of traditional methods and demonstrating why machine learning algorithms could potentially be a solution, the challenge is tackled in the next sections.

1.2. Conventional methods for structural health prediction

Traditional methods for predicting the health of aircraft structures often depend on computationally intensive models. El Hajj Chehade and Younes [9] reviewed various software and calculation tools used for structural reliability and health prediction. Following Spencer et al. [1] the structural-health metric adopted here is $\mathcal{H} = 1 - \max(\mathrm{FI}_j)$, where FI_j are the five failure indices defined in Section 2.3; $\max(\mathrm{FI}_j) = 0$ denotes pristine integrity, while $\max(\mathrm{FI}_j) \geq 1$ coincides with failure. One common method is strength-to-failure analysis, which calculates the load required to cause complete failure in an undamaged wing box. By comparing this value to the expected maximum loads during operation, an estimate of the structural health can be made. Fanteria and Panettieri [10] introduced a constitutive model for the non-linear shear behavior of composite laminates, developed using a user-defined Fortran routine, which can be used in Abaqus non-linear FE code.

Carrera Unified Formulation (CUF) is inherently very versatile and can treat various structural configurations, including beams, plates, and shells. This approach is of great advantage over the usual layer-wise or equivalent single-layer approach alternatives and allows a unified representation for the displacement field up to a series of expansion functions, offering several advantages, such as high-order accuracy [11], geometric flexibility, non-linearity modeling [12,13], and computational efficiency.

Statistical techniques can also be used for health prediction by analyzing historical data on wing box failures and relating them to factors such as operational usage or manufacturing defects; this allows for the development of empirical models for health prediction. Teng [14] discussed conventional methods for predicting fatigue life, which can be categorized into energy-based theory from stress and strain, crack initiation or crack growth models from microscopy measurements, and probability distribution of fatigue life controlled by defects. Ma et al. [15] proposed an approach based on probabilistic consistency and Weibull distribution theory to address the impact of randomness and uncertainty during the fatigue failure process of composite materials.

1.3. Machine learning algorithms for structural health monitoring

Conventional methods for the prediction of the structural health of composite wing boxes can become computationally very expensive, and the trends of the complicated behavior taken by these materials cannot be captured. In that respect, machine learning algorithms appear as a potential substitute process. While traditional techniques are based on predefined models, ML algorithms learn complex relationships directly from data. This data may contain a large diversity of factors, from damage characteristics – like size, location, and type – to material properties of the composite structure, sensor readings monitoring the health of the wing box, and damage condition data from simulations or past failures. Kong et al. [16] reviewed the use of traditional ML models such as the Support Vector Machine (SVM) algorithm, the K-nearest-neighbor (KNN) algorithm, and the elastic net model for structural health prediction. Ribeiro Junior and Gomes [17] discussed using ML to handle the excessive data extracted from the complex techniques employed in the structural health assessment of composite structures. Dadras Eslamlou and Huang [18] presented a systematic review of deploying ML algorithms in civil SHM.

Furthermore, ML algorithms offer adaptability – the ability to be continuously trained on new data. This property allows them to adapt to variations in material properties, which is particularly beneficial when addressing the inherent heterogeneity of composite materials. Altabey and Noori [19] discussed the importance of developing and introducing AI-based methodologies for the SHM of infrastructure systems and the analysis and feature extraction of sensor data, highlighting the superiority of AI-based methodologies in system identification, feature extraction, damage identification, and even direct response prediction of dynamical systems. Jia and Li [20] analyzed several articles through a systematic literature review to investigate the application of Deep Learning (DL) for SHM in the operation and maintenance phase of facilities from three perspectives: data, DL algorithms, and applications. Nguyen-Tran et al. [21] discussed using a combination of deep neural networks for damage detection in structural health monitoring. Chang et al. [22] proposed an AI-based structural health monitoring strategy based on neural network modeling. Kekez and Kubica [23] discussed the proposal for a mixed design of composite materials combined with the application of precisely trained ML models.

Alaimo et al. [24] investigated an ML algorithm that can detect and localize damage without prior knowledge of its characteristics, serving as a real-time data processor for SHM systems. Casaburo et al. [25] developed and validated an ML-based tool for designing global vibroacoustic treatments based on foam cores with embedded periodic patterns, allowing passive control of acoustic paths in layered concepts. Azad and Kim [5] used hybrid deep convolutional networks to present a

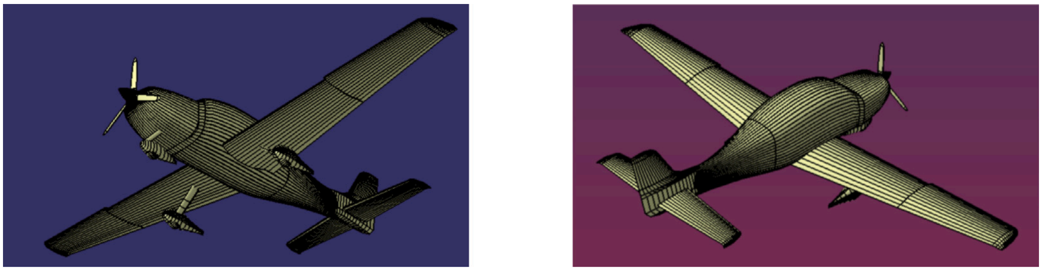
(a) Front.   (b) Rear.

Fig. 1. Cirrus SR22 aircraft CAD isometric views.

robust autonomous damage diagnosis method for laminated composite structures. Wang et al. [26] predicted the failure factors of composite pressure vessels using a combined FEM simulation and machine learning approach. Recent studies [27] have demonstrated that surrogate models that are data-driven can be trained to generalize beyond their learning micro-structure and forecast accurately for unprecedented elastic and volume-fraction regimes by taking physical bounds into account in the learning process.

2. Methodological framework

What follows is a description of the methodological framework, structured in two phases: the acquisition and preprocessing of data and the development of the ML architecture.

1. The initial phase is the data collection and their preparation in training the machine learning model. It includes wing box geometry, material properties, structural health data that can be generated based on detailed FE analyses.
2. The second stage designs a machine learning model and trains it with an explanation, showing the architecture used. Training the model involves inputting the preprocessed data and iteratively fine-tuning the model's inner parameters to decrease the prediction error for the structural health condition.

2.1. Geometry and material properties

The first step in data acquisition is the part associated with the geometry and material properties of the composite wing box, which acts as a reference component. This information feeds with basic data to the ML model for learning the signature of the specific structure under test. In particular, the wing box FE model is drawn from a part extracted from the CAD model of a Cirrus SR22 aircraft shown in Fig. 1, which is freely available online. The Cirrus SR22 is a single-engine, low-wing commercial aircraft developed by the American company Cirrus Aircraft Corporation. Being a development of the Cirrus SR20, the SR22 has had tremendous sales worldwide, especially to newcomers in small aircraft. Compared with the SR20, from which it borrowed its structure, the SR22 Cirrus really does sport an increased wingspan of about 1 m and slightly modified wings, a 310 hp engine, reinforced landing gear, and fully electronic instrumentation. The Cirrus SR22 is a monoplane with a low wing entirely made of composite materials.

The layering sequence and possible delamination phenomena are not taken into consideration to remove one more variable from the ML algorithm. This assumption means that, for the numerical simulations, the composite materials involved are not considered as real lay-ups but rather as equivalent orthotropic layers. Nine different composite materials are considered in their fabric or unidirectional (ud) texture, whose mechanical and inertial properties are shown in Tables 2 and 3, respectively. Additionally, the ultimate strength values are provided in Table 4, where:

- S_{11+} is the value of stress component σ_{11} at longitudinal tensile failure;
- S_{11-} is the value of stress component σ_{11} at compressive tensile failure;
- S_{22+} is the value of stress component σ_{22} at longitudinal tensile failure;
- S_{22-} is the value of stress component σ_{22} at compressive tensile failure;
- S_{12} is the absolute value of stress component σ_{12} at longitudinal shear failure;
- S_{23} is the absolute value of stress component σ_{23} at transverse shear failure.

Table 2
Equivalent orthotropic mechanical properties of analyzed composite materials.

Material	Young modulus [Pa]		
	E_{11}	E_{22}	E_{33}
Carbon fiber (fabric)	7.00E+10	7.00E+10	5.19E+09
Epoxy glass (fabric)	2.50E+10	2.50E+10	5.00E+09
Kevlar (fabric)	3.00E+10	3.00E+10	2.40E+09
Carbon fiber (ud)	1.35E+11	1.00E+10	1.00E+10
High-modulus carbon fiber (ud)	1.75E+11	8.00E+09	8.00E+09
M55 (ud)	3.00E+11	1.20E+10	1.20E+10
Epoxy glass (ud)	4.00E+10	8.00E+09	8.00E+09
Kevlar (ud)	7.50E+10	6.00E+09	6.00E+09
Boron (ud)	2.00E+11	1.50E+10	1.50E+10
Material	Shear modulus [Pa]		
	G_{12}	G_{13}	G_{23}
Carbon fiber (fabric)	5.00E+09	2.29E+09	2.29E+09
Epoxy glass (fabric)	4.00E+09	1.98E+09	1.98E+09
Kevlar (fabric)	5.00E+09	9.52E+08	9.52E+08
Carbon fiber (ud)	5.00E+09	5.00E+09	3.60E+09
High-modulus carbon fiber (ud)	5.00E+09	5.00E+09	2.88E+09
M55 (ud)	5.00E+09	5.00E+09	4.32E+09
Epoxy glass (ud)	4.00E+09	4.00E+09	3.02E+09
Kevlar (ud)	2.00E+09	2.00E+09	2.08E+09
Boron (ud)	5.00E+09	5.00E+09	5.77E+09
Material	Poisson ratio		
	ν_{12}	ν_{13}	ν_{23}
Carbon fiber (fabric)	0.1	0.13	0.13
Epoxy glass (fabric)	0.2	0.26	0.26
Kevlar (fabric)	0.2	0.26	0.26
Carbon fiber (ud)	0.3	0.3	0.39
High-modulus carbon fiber (ud)	0.3	0.3	0.39
M55 (ud)	0.3	0.3	0.39
Epoxy glass (ud)	0.25	0.25	0.325
Kevlar (ud)	0.34	0.34	0.442
Boron (ud)	0.23	0.23	0.299

Mechanical and inertial property values in Tabs. from 2 to 4, are derived from vendor technical data sheets for the reinforcement fibers – Hexcel® T700S standard-modulus carbon [28], Toray® M55J

Table 3

Inertial properties of analyzed composite materials.

Material	Density [kg/m^3]
Carbon fiber (fabric)	1600
Epoxy glass (fabric)	1900
Kevlar (fabric)	1400
Carbon fiber (ud)	1600
High-modulus carbon fiber (ud)	1600
M55 (ud)	1650
Epoxy glass (ud)	1900
Kevlar (ud)	1400
Boron (ud)	2000

Table 4

Equivalent orthotropic ultimate strengths of analyzed composite materials.

Material	Ultimate strength [Pa]					
	S_{11+}	S_{11-}	S_{22+}	S_{22-}	S_{12}	S_{23}
Carbon fiber (fabric)	6.00E+08	5.70E+08	6.00E+08	5.70E+08	9.00E+07	4.13E+07
Epoxy glass (fabric)	4.40E+08	4.25E+08	4.40E+08	4.25E+08	4.00E+07	1.98E+07
Kevlar (fabric)	4.80E+08	1.90E+08	4.80E+08	1.90E+08	5.00E+07	9.52E+06
Carbon fiber (ud)	1.50E+09	1.20E+09	5.00E+07	2.50E+08	7.00E+07	5.04E+07
High-modulus carbon fiber (ud)	1.00E+09	8.50E+08	4.00E+07	2.00E+08	6.00E+07	3.45E+07
M55 (ud)	1.60E+09	1.30E+09	5.00E+07	2.50E+08	7.50E+07	6.47E+07
Epoxy glass (ud)	1.00E+09	6.00E+08	3.00E+07	1.10E+08	4.00E+07	3.02E+07
Kevlar (ud)	1.30E+09	2.80E+08	3.00E+07	1.40E+08	6.00E+07	6.24E+07
Boron (ud)	1.40E+09	2.80E+09	9.00E+07	2.80E+08	1.40E+08	1.62E+08

high-modulus carbon [29], DuPont™ Kevlar® 49 aramid [30], Owens-Corning E-glass [31] and Specialty Materials SCS-6 boron fiber [32], combined with a room-temperature toughened epoxy matrix whose Young's modulus is 2.9 GPa and Poisson ratio 0.34 [33]. Longitudinal constants (E_{11}, G_{12}) are calculated by the Voigt rule-of-mixtures, assuming a conservative fiber volume fraction $V_f = 0.60$ for unidirectional tapes and $V_f = 0.45$ for balanced fabrics; transverse and through-thickness moduli are obtained from the Halpin–Tsai relations, and in-plane Poisson ratios from the inverse rule-of-mixtures. This "equivalent-ply" abstraction is routinely adopted during blended-laminate optimization of transport-class wings [34]. Furthermore, material axes Direction 1 coincides with the local chord (global x for ribs, global z for skins and spars), Direction 2 with the local span (global x for skins, global y for ribs and spars) and Direction 3 with the ply through-thickness (global x for spars, global y for skins, global z for ribs); this frame is retained throughout the FE model and in every failure-index evaluation. By integrating this vast amount of geometric and material property data, the ML model can provide the correlations between the physical attributes of the composite wing box and its structural health.

2.2. *Numerical model characteristics, constraints and loads*

The component extracted from the reference aircraft features two half-wing bays (a portion of the half-wing bounded by three ribs). The thicknesses of the main components of the reference wing box, including ribs, skins, and spars, are 2.5 mm, 2.0 mm, 3.0 mm, respectively. Fig. 2 presents both solid and transparent isometric views of the wing box being considered for the analysis.

According to Fig. 3(a), the boundary conditions are determined by the fixed constraint applied at the external surface of Rib 3 by numerating from 1 to 3, starting from the nearest rib. Distributed static loads that have been exerted on the outer surface of Rib 1 are shown in Fig. 3(b), a graphical description of the most critical operating condition that is known with the aid of the flight envelope plot, which shows the stall speed, maximum maneuver point, and consequently the operating speed region. The above-mentioned load components are estimated to be: $F_x = 0\,\mathrm{N}$, $F_y = -1774.88\,\mathrm{N}$, $F_z = 21\,124.1\,\mathrm{N}$, $M_x = -43\,640.3\,\mathrm{N\,m}$, $M_y = 5352.03\,\mathrm{N\,m}$, $M_z = 389.231\,\mathrm{N\,m}$; for the purpose of failure indices estimation, these values are increased by a safety factor equal to 1.5. Furthermore, a gravity load equal to $-9.81\,\frac{\mathrm{m}}{\mathrm{s}^2}$ directed along z-axis is applied on the whole model.

With the objective to identify of the optimal number of nodes and elements, a systematic refinement analysis is carried out on the undamaged standard-modulus carbon-fiber configuration. Five uniform meshes (element edge 12, 10, 8, 6 and 4 mm) made of linear hexahedral elements of type C3D8R are generated and the peak von-Mises stress $\sigma_{vM}^{\max}$ at the clamped rib and the mid-span vertical deflection w_y are recorded. Convergence is attained when the relative change between successive meshes dropped below ∼1%. Both quantities satisfied this criterion at the 16 860-node and 8592-element mesh adopted throughout the study, confirming numerical sufficiency.

2.3. *Adopted failure criteria*

This research targets five classic failure indices, all designed for composite materials and capturing, from different viewpoints, the stress state information about the analyzed component. Each laminate is idealized as a single equivalent orthotropic ply matching the full stacking sequence. All five criteria are therefore evaluated on the homogenized stress components: a widely adopted preliminary-design simplification that remains conservative provided the lay-up does not introduce strong coupling effects. In the following, the detailed failure criteria are given.

- The Max Stress Criterion identifies composite material failure caused by three possible modes of loading: longitudinal failure, transverse failure, and shear failure:

    - Longitudinal failure occurs whenever $\sigma_{11} \geq S_{11}^{+}$ or $\sigma_{11} \leq S_{11}^{-}$;
    - Transverse failure occurs whenever $\sigma_{22} \geq S_{22}^{+}$ or $\sigma_{22} \leq S_{22}^{-}$;
    - Longitudinal shear failure occurs whenever $|\sigma_{12}| \geq |S_{12}|$.

  Failure Index = Max. Absolute Value of $\left(\frac{\sigma_{11}}{S_{11}^{+}}, \frac{\sigma_{11}}{S_{11}^{-}}, \frac{\sigma_{22}}{S_{22}^{+}}, \frac{\sigma_{22}}{S_{22}^{-}}, \frac{\sigma_{12}}{S_{12}}\right) \geq 1$.
- The Tsai–Wu Criterion is a quadratic, interactive stress-based criterion that identifies failure but does not distinguish between different failure modes. Failure occurs whenever the following condition is satisfied: $F_1\sigma_{11} + F_2\sigma_{22} + F_{11}\sigma_{11}^2 + F_{22}\sigma_{22}^2 + F_{66}\sigma_{12}^2 + 2F_{12}\sigma_{11}\sigma_{22} \geq 1$. The various coefficients F_i and F_{ij} of the Tsai–Wu criterion are defined in terms of known/measured strengths of the composite material: $F_1 \equiv \frac{1}{S_{11}^{+}} - \frac{1}{S_{11}^{-}}$; $F_2 \equiv \frac{1}{S_{22}^{+}} - \frac{1}{S_{22}^{-}}$; $F_{11} \equiv \frac{1}{S_{11}^{+}S_{11}^{-}}$; $F_{22} \equiv \frac{1}{S_{22}^{+}S_{22}^{-}}$; $F_{66} \equiv \frac{1}{S_{12}S_{12}}$. The interaction coefficient F_{12} is computed as $F_{12} = f\sqrt{F_{11}F_{22}}$, where f is a user-specified constant, $-0.5 \leq f \leq 0$.
- The Tsai–Hill criterion is a quadratic, interactive stress-based criterion that identifies failure but does not distinguish between different failure modes. Failure occurs whenever the following condition is satisfied: $\frac{\sigma_{11}^2}{S_{11}^2} - \frac{\sigma_{11}\sigma_{22}}{S_{11}^2} + \frac{\sigma_{22}^2}{S_{22}^2} + \frac{\sigma_{12}^2}{S_{12}^2} \geq 1$.
- The Hashin criterion identifies four different failure modes for the composite material. The four modes are tensile fiber failure, compressive fiber failure, tensile matrix failure, and compressive matrix failure.

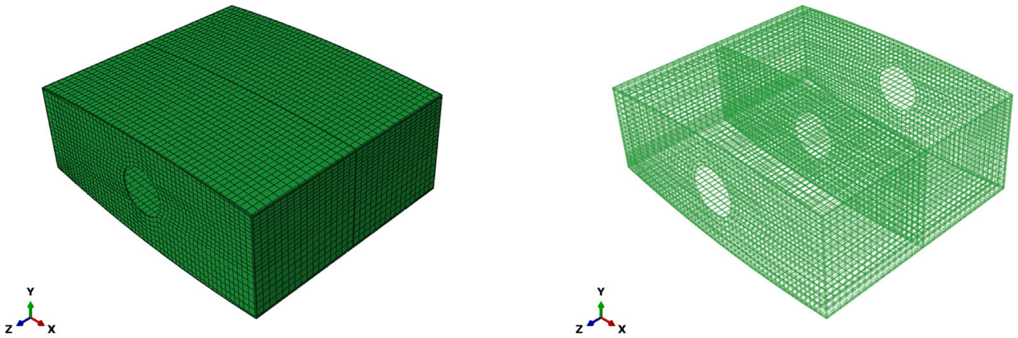

(a) Solid.

(b) Transparent.

Fig. 2. Reference wing box isometric views.

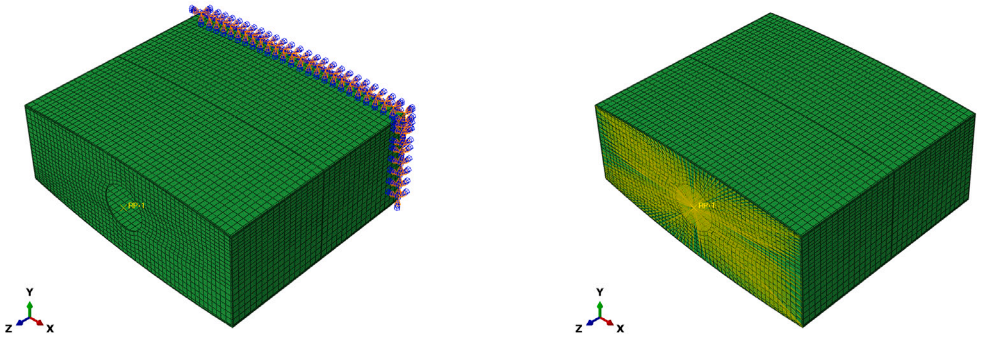

(a) Fixed constraint applied on the external surface of Rib 3, where the critical element is located.

(b) Distributed static loads applied on the external surface of Rib 1.

Fig. 3. Boundary conditions and external loads applied on the reference wing box. The explicit mapping of material axes to the global frame is reported in Section 2.

  - If $\sigma_{11} \geq 0$, the Tensile fiber failure criterion is: $\left(\frac{\sigma_{11}}{S_{11}^{+}}\right)^2 + \alpha\left(\frac{\sigma_{12}^2+\sigma_{13}^2}{S_{12}^2}\right) \geq 1$;
  - If $\sigma_{11} < 0$, the compressive fiber failure criterion is: $\left(\frac{\sigma_{11}}{S_{11}^{-}}\right)^2 \geq 1$;
  - If $\sigma_{22} + \sigma_{33} \geq 0$, the tensile matrix failure criterion is: $\frac{(\sigma_{22}+\sigma_{33})^2}{S_{22}^{+2}} + \frac{\sigma_{23}^2-\sigma_{22}\sigma_{33}}{S_{23}^2} + \frac{\sigma_{12}^2+\sigma_{13}^2}{S_{12}^2} \geq 1$;
  - If $\sigma_{22} + \sigma_{33} < 0$, the compressive matrix failure criterion is: $\left[\left(\frac{S_{22}^{-}}{2S_{23}}\right)^2 - 1\right]\left(\frac{\sigma_{22}+\sigma_{33}}{S_{22}^{-}}\right) + \frac{(\sigma_{22}+\sigma_{33})^2}{4S_{23}^2} + \frac{\sigma_{23}^2-\sigma_{22}\sigma_{33}}{S_{23}^2} + \frac{\sigma_{12}^2+\sigma_{13}^2}{S_{12}^2} \geq 1.$

  The Hashin equations require a user-specified parameter α; the allowable range is $0 \leq \alpha \leq 1$, and the default value is $\alpha = 0$.

- The Christensen criterion identifies two failure modes: matrix failure and fiber failure:
  - The matrix failure criterion is: $\left(\frac{1}{S_{22}^{+}} - \frac{1}{S_{22}^{-}}\right)(\sigma_{22}+\sigma_{33}) + \frac{1}{S_{22}^{+}S_{22}^{-}}(\sigma_{22}+\sigma_{33})^2 + \frac{1}{S_{23}^2}(\sigma_{23}^2 - \sigma_{22}\sigma_{33}) + \frac{1}{S_{12}^2}(\sigma_{12}^2+\sigma_{13}^2) \geq 1$;
  - The fiber failure criterion is: $\left(\frac{1}{S_{11}^{+}} - \frac{1}{S_{11}^{-}}\right)\sigma_{11} + \frac{\sigma_{11}^2}{S_{11}^{+}S_{11}^{-}} \geq \mathbf{1}$.

The five criteria are not embedded in a user-defined material (UMAT) model. Instead, for every load case, the six stress components of every integration point that maximizes the von-Mises equivalent stress are exported to the output database (ODB), and a dedicated spreadsheet computes the failure indices in post-processing, thereby obviating the need for an explicit UMAT while markedly accelerating the parametric study. The surrogate is thus trained on the scalar value $\max(\mathrm{FI}_j)$, consistently with intralaminar failure certification philosophy.

2.4. FE analyses for damage condition data generation

To train the ML model, there is a need to have reliable data on the damage condition of the composite wing box. The traditional way of testing through experiments is time-consuming and expensive. For this research, FE analyses are utilized as a type of 'Virtual Testing' to generate the necessary data. In this case, the FE method establishes a digital model of composite wing box featuring damage. Such a FEM digital model is known as a fine model as it provides information regarding geometry used along with the material characters applied.

Different models for behavior simulation of wing box have been considered with nine types of composite materials. These simulations provide valuable insight into the damage condition of the structure, which, in the form of failure indices, serve as the target output during the training process for the ML model. FE analyses act as a virtual testing environment in which the data required regarding damage condition are obtained to train the ML model, allowing for the prediction of the structural health for intralaminar damaged configurations.

The reference wing box is modeled with the nine composite materials in undamaged and damaged conditions. Damage is characterized by the scalar intensity

$$D_I = 1 - \frac{E_{ij}^{\mathrm{dam}}}{E_{ij}^{\mathrm{und}}}, \tag{1}$$

where E_{ij}^{und} is the pristine generic mechanical modulus and E_{ij}^{dam} its reduced counterpart inside the damaged patch. The four prescribed levels $D_I \in \{0.20, 0.40, 0.60, 0.80\}$ correspond to the stiffness-reduction

Table 5

Damage cases for the parametric analysis aiming at a material-oriented database.

Case	Location	Extent [m^2]
1	Rib	2.72E−04
2	Rib	1.09E−03
3	Rib	2.72E−04
4	Rib	1.09E−03
5	Rib	2.72E−04
6	Rib	1.09E−03
7	Rib	2.72E−04
8	Rib	1.09E−03
9	Rib	2.72E−04
10	Rib	1.09E−03
11	Rib	2.72E−04
12	Rib	1.09E−03
13	Skin	1.80E−03
14	Skin	4.99E−03
15	Skin	1.80E−03
16	Skin	4.99E−03
17	Skin	1.80E−03
18	Skin	4.99E−03
19	Skin	1.80E−03
20	Skin	4.99E−03
21	Spar	7.99E−04
22	Spar	3.19E−03
23	Spar	7.99E−04
24	Spar	3.19E−03
25	Spar	7.99E−04
26	Spar	3.19E−03
27	Spar	7.99E−04
28	Spar	3.19E−03

intervals normally adopted in continuum-damage mechanics studies of fiber reinforced polymers (FRP) laminates. Each of the 28 rectangular patches listed in Table 5 is centered on the geometric mid-surface of the indicated rib, skin or spar to preserve load symmetry, leading to a total of 9 undamaged cases and 1008 damaged ones.

Results are extracted in terms of six direct stress components at the centroid of the most-stressed element of the model, which, as expected, is located along the fixed rib. However, the stress field in this part of the model is actually little affected by any intralaminar damage conditions. The phenomenon does not constitute a problem in this context because the interest for this parametric analysis is restricted to the capability of the ML algorithm in unveiling dependence of the five selected failure indices of the most stressed element, computed based on the six direct stress components detailed in Section 2.3, on the choice of material rather than the intralaminar damage conditions. However, considering various conditions of intralaminar damage raises the population of data in the numerical database; otherwise, the algorithm of ML would have only nine undamaged cases for training and testing. The results obtained regarding the failure indices of nine composite materials in an undamaged state are summarized in Fig. 4.

2.5. Machine learning

In this section, the data obtained from the FEM analysis conducted using the methodology discussed earlier are used to input into the classical ML pipeline (Fig. 5). The dataset captures the relationships between input parameters, specifically material properties and loading conditions, and the corresponding output, which includes the components of the stress tensor and failure indices computed using various criteria.

The aim of the ML approach is to establish a predictive model capable of accurately estimating the failure index of structural components based on these input parameters.

To ensure the development of a reliable and generalizable ML model, the following systematic pipeline made up of four stages will be adopted:

- Exploratory Data Analysis (EDA): the EDA phase involves a thorough investigation of the dataset to uncover patterns, assess the distribution of key variables, and identify potential issues such as outliers or missing values.
- Data Preparation: In this step, data preprocessing techniques are applied, including feature selection, normalization, and encoding of categorical variables. Careful consideration is given to ensure that the prepared dataset is both representative and suitable for ML model training.
- Model Development: Various ML algorithms will be explored and optimized to identify the most suitable predictive model. This phase includes hyper-parameter tuning and training–validation strategies to maximize model performance.
- Validation and Evaluation: Finally, the developed model will be rigorously evaluated using appropriate metrics, ensuring its applicability and reliability to estimate structural component failure indices.

The framework is designed to enable scalable and efficient predictions, contributing to the broader goal of optimizing structural component design and maintenance strategies.

2.5.1. Exploratory data analysis

Exploratory Data Analysis (EDA) serves as a critical preliminary step in understanding the intrinsic characteristics and potential insights hidden within a dataset. In order to do that different analysis and visualizations have been performed.

Statistical analyses are conducted on the data collected in Secs. from 2.1 to 2.3. Table 6 reports the mean and median values of the input features, grouped according to the presence or absence of damage. Tables 7 and 8 present the mean and median values of the output variables, stratified by material type.

Correlation is quantified by the sample Pearson coefficient r_{xy}, which is a measure of strength and direction of the linear relationship between two variables X and Y. It is defined as:

$$r_{xy} = \frac{\mathrm{Cov}(X,Y)}{\sigma_X \sigma_Y} \tag{2}$$

where $\mathrm{Cov}(X,Y)$ stands for the covariance between X and Y, and σ_X, σ_Y are their respective standard deviations. The coefficient takes values in the interval $[-1,1]$, with $r_{xy} = 1$ and $r_{xy} = -1$ indicating perfect positive and negative linear correlation, respectively, and $r_{xy} = 0$ indicating absence of linear correlation.

The correlation matrices between the input quantities – the structural properties of the material and the damage components – and the stress tensor are shown in Fig. 6. A higher correlation is associated with a higher intensity of green (in case of positive correlation) and purple (in case of negative correlation). It can be noted that the data most correlated with the stress tensor are those related to the structural properties of the material.

The correlation matrices between the input quantities – the structural properties of the material and the damage components – and the failure indices considered are shown in Fig. 7. The failure indices seem to have strong correlations with the variables in the dataset, allowing to create a regression model that works directly on these variables.

A probability density function (PDF) describes how the values of a continuous random variable are distributed over its range. PDF is a non-negative function $f(x)$ such that the probability of the variable falling within any given interval corresponds to the area under the curve of $f(x)$ over that interval. The PDF itself does not give the probability of the variable assuming a single exact value, but quantifies the relative likelihood of values in infinitesimally small intervals. PDFs of σ_{11} with respect to the components that characterize the damage (intensity, position and extent) are shown in Fig. 8. Each PDF graph is represented using distinct colors, with each color corresponding to a specific value assumed by one of the damage components. It is evident that, regardless of the specific damage components considered, the trends of the

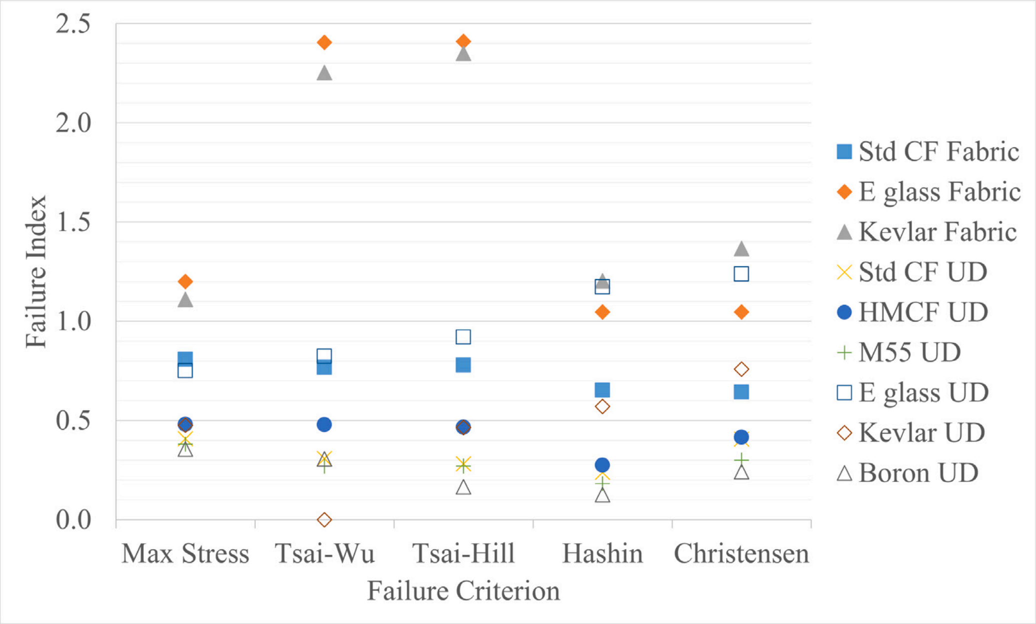

Fig. 4. Five failure indices of the most stressed element, computed for nine undamaged composite materials.

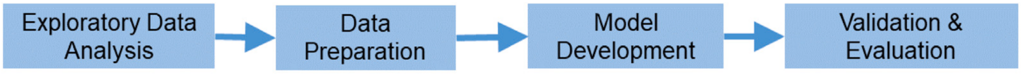

Fig. 5. Classical machine learning pipeline.

Table 6
Material properties with and without damage.

Property	Symbol	Unit	No damage	With damage
Elastic Moduli				
Young's modulus 1	E_1	Pa	$1.17 \times 10^{11} \pm 9.35 \times 10^{10}$	$1.17 \times 10^{11} \pm 8.82 \times 10^{10}$
Young's modulus 2	E_2	Pa	$2.04 \times 10^{10} \pm 2.03 \times 10^{10}$	$2.04 \times 10^{10} \pm 1.92 \times 10^{10}$
Young's modulus 3	E_3	Pa	$7.95 \times 10^{9} \pm 3.89 \times 10^{9}$	$7.95 \times 10^{9} \pm 3.67 \times 10^{9}$
Shear Moduli				
Shear modulus 12	G_{12}	Pa	$4.44 \times 10^{9} \pm 1.01 \times 10^{9}$	$4.44 \times 10^{9} \pm 9.56 \times 10^{8}$
Shear modulus 13	G_{13}	Pa	$3.47 \times 10^{9} \pm 1.65 \times 10^{9}$	$3.47 \times 10^{9} \pm 1.56 \times 10^{9}$
Shear modulus 23	G_{23}	Pa	$2.99 \times 10^{9} \pm 1.43 \times 10^{9}$	$2.99 \times 10^{9} \pm 1.35 \times 10^{9}$
Poisson's ratios				
Poisson's ratio 12	ν_{12}	–	0.247 ± 0.074	0.247 ± 0.069
Poisson's ratio 13	ν_{13}	–	0.263 ± 0.060	0.263 ± 0.057
Poisson's ratio 23	ν_{23}	–	0.321 ± 0.096	0.321 ± 0.090
Strength properties				
Tensile strength 1	S_{1+}	Pa	$1.04 \times 10^{9} \pm 4.46 \times 10^{8}$	$1.04 \times 10^{9} \pm 4.21 \times 10^{8}$
Compressive strength 1	S_{1-}	Pa	$9.13 \times 10^{8} \pm 8.04 \times 10^{8}$	$9.13 \times 10^{8} \pm 7.59 \times 10^{8}$
Tensile strength 2	S_{2+}	Pa	$2.01 \times 10^{8} \pm 2.34 \times 10^{8}$	$2.01 \times 10^{8} \pm 2.20 \times 10^{8}$
Compressive strength 2	S_{2-}	Pa	$2.68 \times 10^{8} \pm 1.45 \times 10^{8}$	$2.68 \times 10^{8} \pm 1.37 \times 10^{8}$
Shear strength 12	S_{12}	Pa	$6.94 \times 10^{7} \pm 3.11 \times 10^{7}$	$6.94 \times 10^{7} \pm 2.93 \times 10^{7}$
Shear strength 23	S_{23}	Pa	$5.28 \times 10^{7} \pm 4.49 \times 10^{7}$	$5.28 \times 10^{7} \pm 4.23 \times 10^{7}$
Physical properties				
Density	ρ	kg/m^3	1672.22 ± 216.67	1672.22 ± 204.39

σ_{11} are almost perfectly overlapping. This indicates that the σ_{11} does not exhibit significant variability as the damage components change. The behavior is the same for all the stress tensor and the failure indices. The lack of noticeable variation or divergence in the failure index and stress tensor trends suggests that the computed values are consistent across different damages. As a result, this uniformity implies that the damage components do not introduce sufficient variance to warrant the development of a predictive or explanatory model based only on these factors.

Instead, it can be observed in Fig. 9 that as the type of materials examined varies, the PDFs assume different shapes and values. The multi-modal appearance of the PDFs arises because each curve is a nine-component mixture, one mode per orthotropic material family. Consequently, the material properties are the factors that most influence the Stress Tensor components and the Failure Indices. The conclusion of the EDA made it possible to advance the hypothesis of developing an ad-hoc model for the prediction of failure indices

Table 7
Stress components results.

Material	Stress components [Pa]					
	σ_{11} Mean ± Std	σ_{22} Mean ± Std	σ_{33} Mean ± Std	σ_{12} Mean ± Std	σ_{13} Mean ± Std	σ_{23} Mean ± Std
Boron UD	3.33×10^8 $\pm 1.67 \times 10^7$	3.29×10^6 $\pm 2.06 \times 10^5$	3.05×10^6 $\pm 2.29 \times 10^5$	1.83×10^7 $\pm 9.03 \times 10^5$	4.61×10^6 $\pm 3.15 \times 10^5$	-4.99×10^5 $\pm 4.51 \times 10^4$
E glass Fabric	3.01×10^8 $\pm 1.52 \times 10^7$	2.36×10^7 $\pm 1.35 \times 10^6$	9.37×10^6 $\pm 4.86 \times 10^5$	3.20×10^7 $\pm 1.66 \times 10^6$	2.88×10^5 $\pm 1.77 \times 10^5$	8.78×10^5 $\pm 5.04 \times 10^4$
E glass UD	2.67×10^8 $\pm 1.36 \times 10^7$	8.74×10^6 $\pm 5.33 \times 10^5$	8.92×10^6 $\pm 5.42 \times 10^5$	2.05×10^7 $\pm 1.03 \times 10^6$	-2.35×10^5 $\pm 1.80 \times 10^5$	1.36×10^5 $\pm 2.09 \times 10^4$
HMCF UD	3.21×10^8 $\pm 1.61 \times 10^7$	3.42×10^6 $\pm 1.54 \times 10^5$	3.04×10^6 $\pm 1.95 \times 10^5$	1.89×10^7 $\pm 9.90 \times 10^5$	4.64×10^6 $\pm 2.94 \times 10^5$	-5.12×10^5 $\pm 3.32 \times 10^4$
Kevlar Fabric	3.53×10^8 $\pm 1.75 \times 10^7$	2.68×10^7 $\pm 1.43 \times 10^6$	4.64×10^6 $\pm 3.11 \times 10^5$	3.76×10^7 $\pm 1.85 \times 10^6$	2.73×10^6 $\pm 1.93 \times 10^5$	3.55×10^5 $\pm 1.79 \times 10^4$
Kevlar UD	3.38×10^8 $\pm 1.69 \times 10^7$	5.93×10^6 $\pm 3.75 \times 10^5$	5.97×10^6 $\pm 3.79 \times 10^5$	1.95×10^7 $\pm 9.31 \times 10^5$	2.60×10^6 $\pm 2.14 \times 10^5$	-1.19×10^5 $\pm 2.81 \times 10^4$
M55 UD	3.70×10^8 $\pm 1.83 \times 10^7$	2.99×10^6 $\pm 1.93 \times 10^5$	2.68×10^6 $\pm 2.21 \times 10^5$	1.91×10^7 $\pm 9.62 \times 10^5$	4.84×10^6 $\pm 2.79 \times 10^5$	-5.86×10^5 $\pm 2.94 \times 10^4$
Std CF Fabric	3.24×10^8 $\pm 1.62 \times 10^7$	9.65×10^6 $\pm 7.39 \times 10^5$	1.69×10^6 $\pm 1.81 \times 10^5$	2.35×10^7 $\pm 1.13 \times 10^6$	5.88×10^6 $\pm 3.40 \times 10^5$	-1.96×10^5 $\pm 1.15 \times 10^4$
Std CF UD	3.09×10^8 $\pm 1.55 \times 10^7$	4.87×10^6 $\pm 3.09 \times 10^5$	4.64×10^6 $\pm 3.41 \times 10^5$	1.92×10^7 $\pm 9.70 \times 10^5$	3.32×10^6 $\pm 1.51 \times 10^5$	-3.43×10^5 $\pm 1.78 \times 10^4$

Table 8
Failure criteria for each material, reported as mean ± standard deviation.

Material	Max stress	Tsai–Wu	Tsai–Hill	Hashin	Christensen
Boron UD	0.240 ± 0.012	0.189 ± 0.013	0.071 ± 0.010	0.060 ± 0.008	0.150 ± 0.009
E-glass Fabric	0.799 ± 0.041	1.062 ± 0.135	1.078 ± 0.134	0.466 ± 0.059	0.462 ± 0.059
E-glass UD	0.509 ± 0.027	0.385 ± 0.044	0.416 ± 0.051	0.524 ± 0.065	0.696 ± 0.055
HMCF UD	0.322 ± 0.016	0.223 ± 0.026	0.213 ± 0.026	0.122 ± 0.016	0.231 ± 0.018
Kevlar Fabric	0.750 ± 0.037	0.633 ± 0.163	1.070 ± 0.129	0.539 ± 0.067	0.248 ± 0.113
Kevlar UD	0.324 ± 0.017	0.000 ± 0.000	0.212 ± 0.025	0.259 ± 0.032	0.442 ± 0.034
M55 UD	0.253 ± 0.013	0.121 ± 0.015	0.121 ± 0.015	0.081 ± 0.010	0.161 ± 0.014
Std CF Fabric	0.542 ± 0.027	0.336 ± 0.044	0.354 ± 0.043	0.293 ± 0.036	0.282 ± 0.036
Std CF UD	0.274 ± 0.015	0.151 ± 0.016	0.131 ± 0.015	0.102 ± 0.014	0.230 ± 0.018

from structural characteristics of the material enriched with different combination of the damage components.

2.5.2. Data preparation

In materials science and composite material failure prediction, meticulous feature engineering and selection have been crucial for developing robust predictive models. Given the limited dataset dimensions encompassing various fabric and unidirectional materials, a comprehensive preprocessing strategy has been adopted to maximize model performance and generalizability.

Normalization and feature selection have been conducted on the entire dataset. This approach has been necessitated by the small sample size, which has included only 9 different materials. Instead of developing separate models for fabric and unidirectional materials, a unified modeling strategy has been implemented, creating five distinct models corresponding to different failure indices.

The input features have comprised both numerical and categorical variables. Numerical features have included elastic moduli (E_1, E_2, E_3), shear moduli (G_{12}, G_{13}, G_{23}), Poisson's ratios (ν_{12}, ν_{13}, $\nu 23$), density (ρ), stress components (σ_{11}, σ_{22}, σ_{33}, σ_{12}, σ_{13}, σ_{23}), and additional parameters like extent and intensity. The categorical feature "Position" has represented structural locations (None, Rib, Skin, Spar).

Categorical feature encoding. For the categorical "Position" feature, one-hot encoding has been selected after carefully weighing computational and statistical considerations. One-hot encoding transforms the categorical variable into binary features without introducing arbitrary hierarchical relationships. While this approach increases feature dimensionality, it has proven particularly effective for decision tree-based algorithms by preventing unintended ordinal interpretations of categorical variables.

Numerical feature scaling. Observing multi-modal data distributions, standard normalization techniques that assume Gaussian distributions have been rejected. Min–max scaling has emerged as the optimal preprocessing method. Distinct scaling ranges of [0, 1] for input features and [0, 1.5] for output failure indices have been applied. This approach preserves relative data distances and accommodates potential extreme failure scenarios while maintaining numerical stability.

The [0, 1.5] range for failure indices has strategically allowed representation of standard failure conditions (0–1) and exceptional cases up to 1.5. This scaling strategy ensures that the models can capture nuanced failure mechanisms without arbitrary truncation.

Feature selection strategy. A correlation-based feature selection methodology has been implemented to identify the most informative predictors. Certain features, including position-related binary indicators, extent, and intensity, have been consistently retained. For the remaining features, a progressive correlation ranking approach using Pearson correlation coefficients has been implemented.

The feature selection process has involved computing correlation matrices for each failure index and systematically reducing the correlation threshold. Starting from a maximum correlation of 1.0 and decrementing by 0.03 in each iteration, two to three most correlated input features have been selected. This method ensures that the most statistically significant predictors have been retained while mitigating multi-collinearity, ultimately developing a flexible preprocessing framework capable of capturing complex material behavior across diverse composite systems.

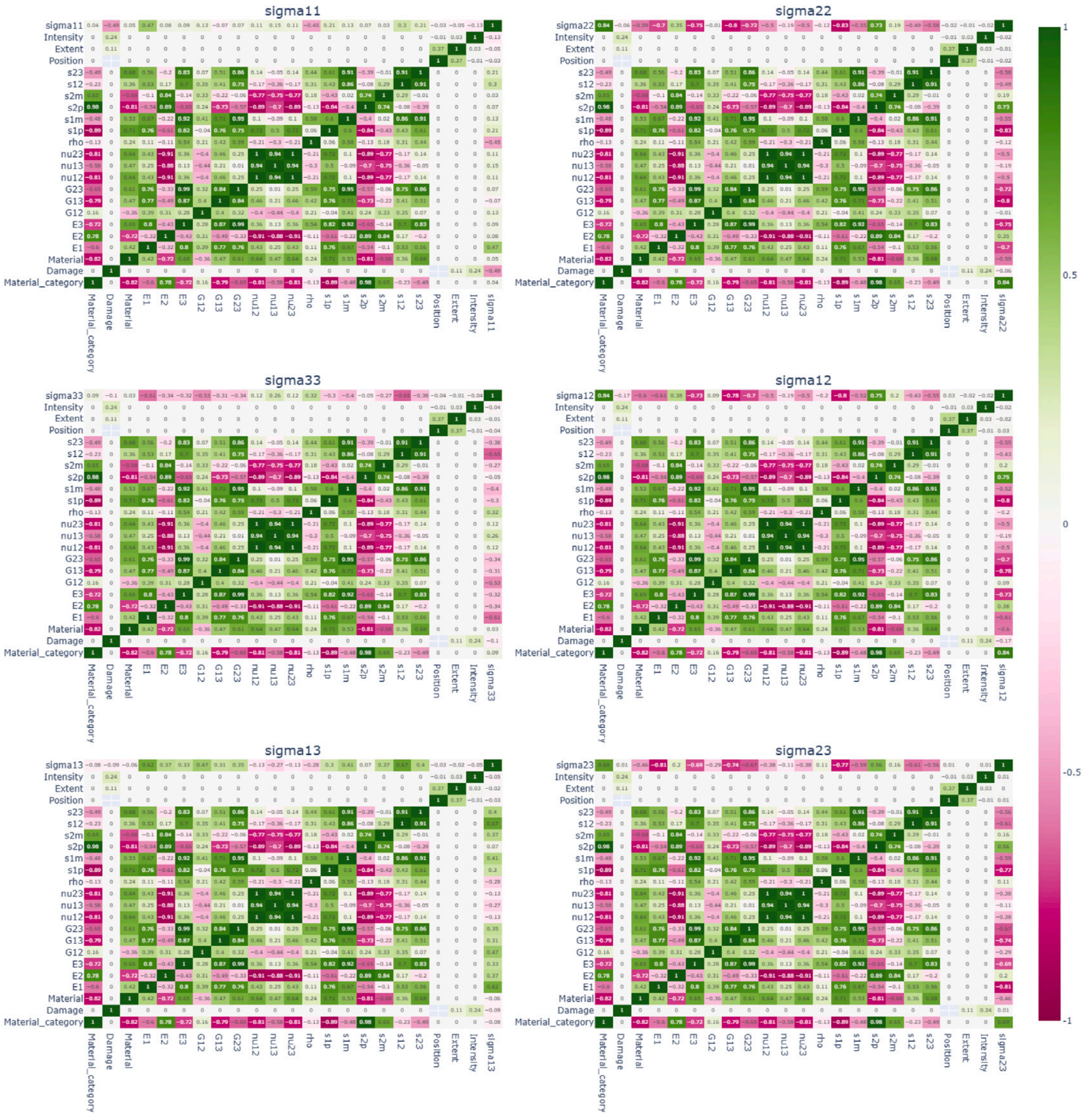

Fig. 6. Correlation matrices between the input quantities – the structural properties of the material and the damage components – and the stress tensor.

2.5.3. Model development

Two powerful regression algorithms, Random Forest and Support Vector Regression, have been selected for predictive modeling, primarily due to the limited dimensionality of the available dataset. Given the restricted sample size, traditional machine learning algorithms have been preferred over deep neural networks to mitigate the risk of overfitting and ensure more reliable model generalization. Models are both implemented using `scikit-learn`.

In Random Forest regression an ensemble of N_{t} binary decision trees $h(x, \Theta_k)$ is grown on bootstrap replicas of the training set; each split considers a random subset of m_{try} features, and the surrogate prediction is the simple average $\hat{y} = N_{\mathrm{t}}^{-1} \sum_{k=1}^{N_{\mathrm{t}}} h(x, \Theta_k)$. Support Vector Regression seeks a function $f(x) = \sum_{i=1}^{\ell} \alpha_i K(x_i, x) + b$ that minimizes $\frac{1}{2}\|\alpha\|^2$ subject to an ε-insensitive tube around the targets, where

- N_{t} is the total number of decision trees that constitute the Random Forest ensemble;
- m_{try} is the cardinality of the random subset of features examined at each node split in a tree;
- $h(x, \Theta_k)$ is the prediction returned by the kth tree for input x, parametrized by node-split set Θ_k;
- $\hat{y}$ is the ensemble-averaged Random Forest prediction;
- ε is the half-width of the ε-insensitive loss tube in SVR;
- γ is the inverse squared length-scale controlling the spread of the radial-basis kernel;
- $f(x)$ is the regression function learned by SVR, $f(x) = \sum_{i=1}^{\ell} \alpha_i K(x_i, x) + b$;
- α_i is the dual Lagrange multiplier (weight) associated with the ith support vector;
- $K(x_i, x)$ is the kernel function evaluating similarity between training vector x_i and query point x;
- b is the bias (intercept) term in the SVR decision function.

The `RandomForestRegressor` is optimized by varying the following hyper-parameters:

- `n_estimators`: [50, 100, 200] - number of trees in the forest (default: 100);
- `max_depth`: [None, 10, 20, 30] - maximum depth of each tree (default: None);
- `min_samples_split`: [2, 5, 10] - minimum number of samples required to split an internal node (default: 2);
- `min_samples_leaf`: [1, 2, 4] - minimum number of samples required to be at a leaf node (default: 1).

A comprehensive hyperparameter search is performed for both models using `GridSearchCV`. Grid search is an exhaustive parameter

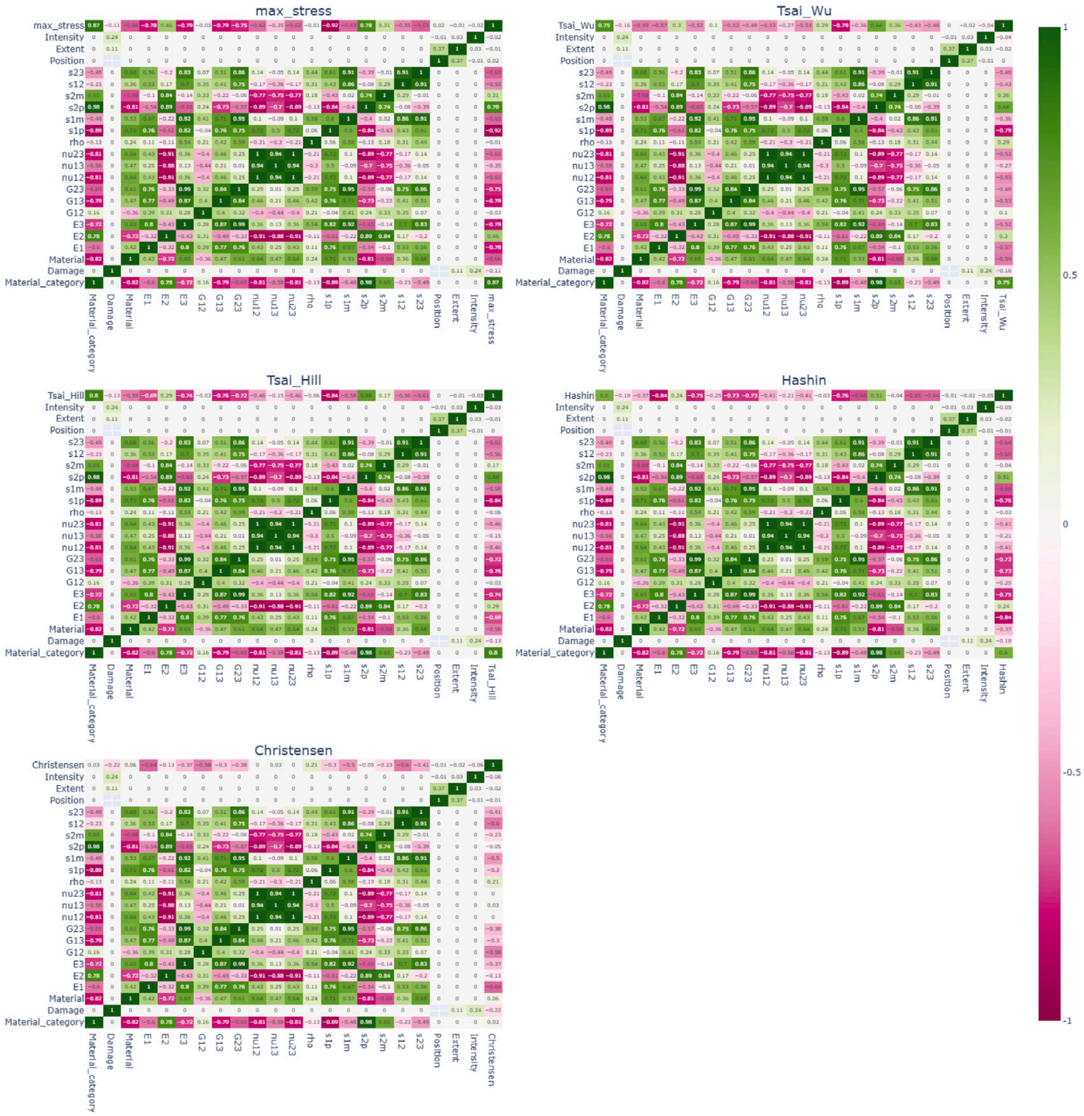

Fig. 7. Correlation matrices between the input quantities – the structural properties of the material and the damage components – and the failure indices.

optimization method that evaluates all possible combinations of hyperparameter values defined within a specified search space. For each configuration, the model is trained and validated using k-fold cross-validation, and its performance is assessed according to a predefined scoring metric. The combination of hyper-parameters that yields the best average performance across folds is automatically selected and retained for the final model. This procedure ensures a systematic exploration of the hyperparameter space and reduces the likelihood of suboptimal tuning due to manual or random selection.

In this work, the scoring function used for hyperparameter selection is the `neg_mean_absolute_error`, due to its robustness to outliers. The coefficient of correlation (r_{xy}) is also computed for evaluation purposes. This approach reduces over-fitting and provides robust predictions by leveraging the wisdom of crowd principle among trees. Each tree is built using a random subset of features and training samples, introducing diversity and reducing variance [35].

Support Vector Regression, derived from Support Vector Machines, operates by transforming the input data into a higher-dimensional space where linear regression becomes possible. The algorithm seeks to find a hyperplane that maximizes the margin around the prediction, using kernel functions to capture complex non-linear relationships. By introducing an epsilon-insensitive zone, SVR allows for a certain degree of error tolerance, making it particularly effective for datasets with limited observations [36]. Specifically, SVR seeks a function $f(x) = \sum_{i=1}^{\ell} \alpha_i K(x_i, x) + b$ that minimizes $\frac{1}{2}\|\alpha\|^2$ while forcing all residuals to lie inside an ε–insensitive tube; training therefore solves a convex quadratic problem whose dual variables α_i correspond to a sparse set of support vectors. For moderately non-linear tabular data the radial-basis kernel $K(x_i, x) = e^{(-\gamma\|x_i - x\|^2)}$, where $\|x_i - x\|$ is the euclidean norm of the difference between feature vectors, is widely accepted because it maps the inputs to an infinite-dimensional Hilbert space without introducing additional hyper-parameters. Recent composites-engineering studies confirm the relevance of this configuration: Bagherzadeh et al. [37] demonstrated that a stacked SVR architecture achieves state-of-the-art accuracy in predicting maximum stress in plain-weave laminates with interacting holes; additionally, a chained ensemble with SVR as meta-learner yielded superior load-capacity and ductility predictions for fiber-reinforced beams [38], thereby reinforcing the relevance of SVR-based surrogates for spatially heterogeneous composite stress prediction. The SVR model is tuned over the following hyperparameter grid:

- `C`: [0.1, 1, 10, 100] - regularization parameter controlling trade-off between training error and model complexity (default: 1);
- `epsilon`: [0.01, 0.1, 0.5] - insensitive zone within which errors are not penalized (default: 0.1);

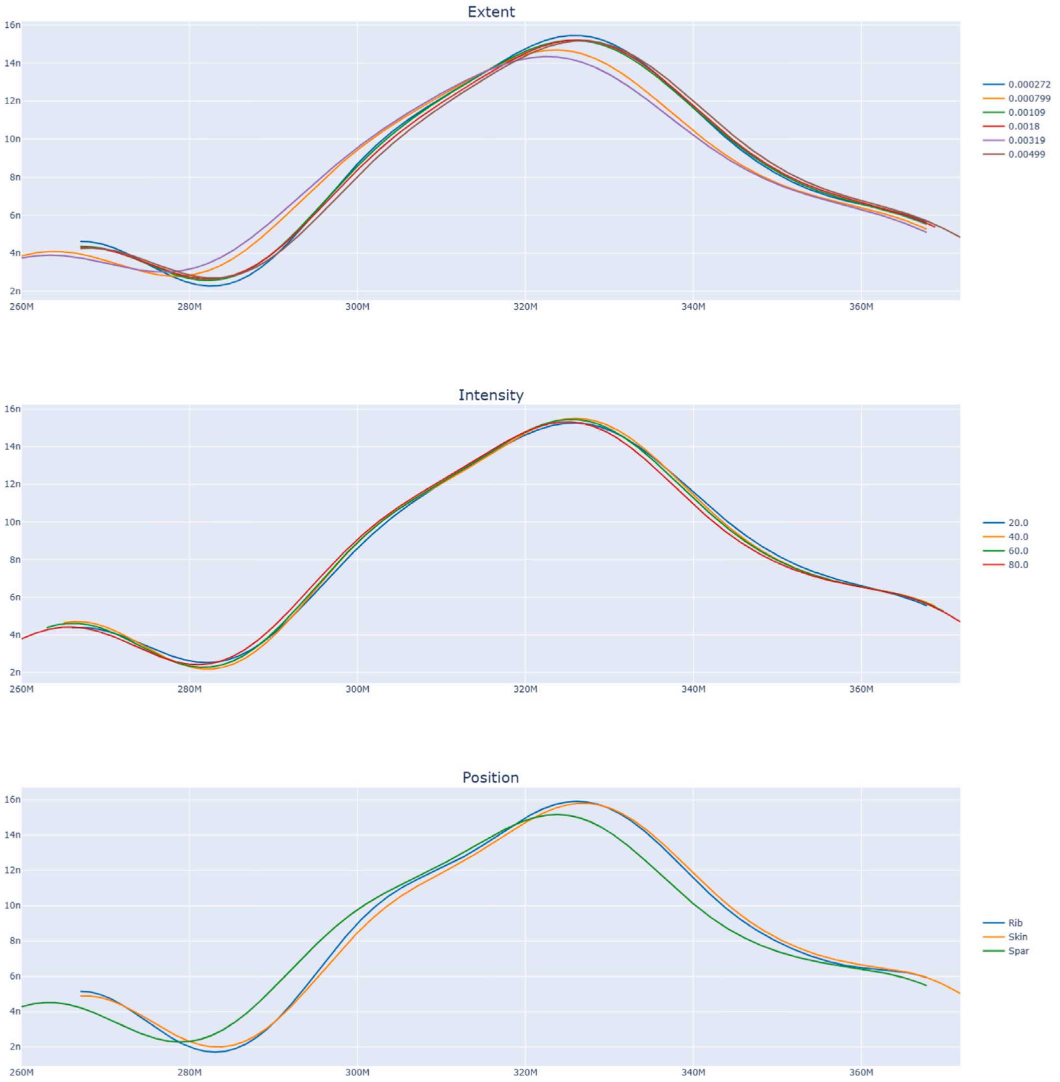

Fig. 8. Kernel-density estimates of σ_{11} for the nine-materials mixture under different damage characteristics (color-coded); see Fig. 9 for the material-wise comparison.

- `gamma`: ['scale', 'auto', 0.01, 0.1] - defines the influence radius of support vectors (default: 'scale');
- `kernel`: ['rbf', 'linear', 'poly'] - kernel function used to project data into higher-dimensional space (default: 'rbf').

The algorithmic palette is deliberately restricted to RF and SVR: empirical benchmarks on more than one hundred tabular datasets show that tree ensembles or kernel machines dominate neural and attention-based architectures whenever the sample size lies below $\sim 10^4$ observations and the feature space is low-to-moderately dimensional [39,40]. Enlarging the pool with deeper models would therefore add computational cost and interpretive burden without a statistically credible expectation of accuracy gain for the 1017 cases available here.

2.5.4. Validation and evaluation

For the training phase, the dataset has been split using two distinct approaches: a 66%–33% split and a LOO cross-validation method. In the 66%–33% split (Fig. 10), the dataset has been partitioned to ensure representation across different materials. For fabric materials, 2 out of 3 have been used for training and 1 for testing, while for unidirectional (UD) materials, 4 out of 6 have been allocated to training and 2 to testing. The specific split has included training materials such as 'Std CF UD', 'Kevlar UD', 'HMCF UD', 'Boron UD', 'E glass Fabric', and 'Std CF Fabric', with test materials comprising 'M55 UD', 'E glass UD', and 'Kevlar Fabric'.

The training methodology has been comprehensive and methodical, with distinct pre-processing and hyper-parameter optimization strategies for each regression algorithm. For each algorithm, two model variants have been developed: one using all available features and another using only the most correlated features. A grid search approach has been employed to optimize hyper-parameters, with different parameter ranges for each algorithm. The Random Forest Regressor has focused on parameters like the number of trees, maximum tree depth, and minimum samples for node splitting, while the SVR has tuned regularization parameters, epsilon values, and kernel functions.

To ensure robust model performance evaluation and minimize potential bias, a LOO cross-validation approach has been implemented. This validation strategy has been specifically designed to address the unique structure of the material-based dataset. In each iteration, the model has been trained on all materials except one, which has subsequently been used as the test set. This method allows for a comprehensive assessment of the model's predictive capabilities across different materials, providing a more nuanced understanding of its generalization potential to make correct prediction on new materials, not included in the dataset.

As shown in Table 9, the LOO procedure has systematically excluded one material at a time, utilizing the remaining materials for

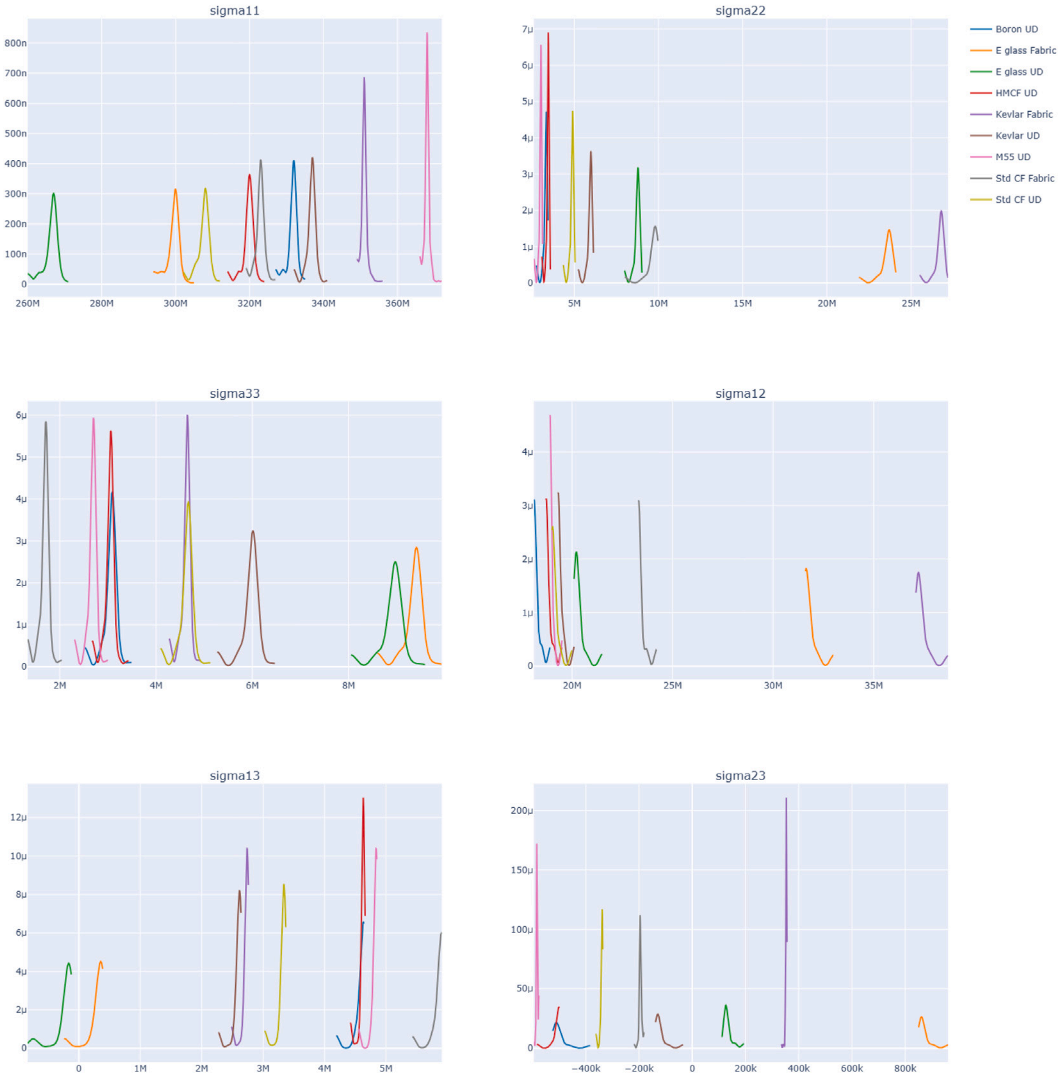

Fig. 9. Comparison of PDFs of stress tensors analyzed across different materials.

Table 9
This table presents the LOO cross-validation training and test set. In each iteration a different material is used as the test set, while the other materials comprise the training set.

Iteration	Training set	Test set
1	Kevlar UD, HMCF UD, Baron UD, E Glass Fabric, Std CF Fabric, Glass UD, Kevlar Fabric, MSS UD	Std CF UD
2	Std CF UD, HMCF UD, Baron UD, E Glass Fabric, Std CF Fabric, Glass UD, Kevlar Fabric, MSS UD	Kevlar UD
3	Std CF UD, Kevlar UD, Baron UD, E Glass Fabric, Std CF Fabric,Glass UD, Kevlar Fabric, MSS UD	HMCF UD
4	Std CF UD, Kevlar UD, HMCF UD, E Glass Fabric, Std CF Fabric,Glass UD, Kevlar Fabric, MSS UD	Baron UD
5	Std CF UD, Kevlar UD, HMCF UD, Baron UD, Std CF Fabric,Glass UD, Kevlar Fabric, MSS UD	E Glass Fabric
6	Std CF UD, Kevlar UD, HMCF UD, Baron UD, E Glass Fabric, Glass UD, Kevlar Fabric, MSS UD	Std CF Fabric
7	Std CF UD, Kevlar UD, HMCF UD, Baron UD, E Glass Fabric, Std CF Fabric, Kevlar Fabric, MSS UD	Glass UD
8	Std CF UD, Kevlar UD, HMCF UD, Baron UD, E Glass Fabric, Std CF Fabric, Glass UD, MSS UD	Kevlar Fabric
9	Std CF UD, Kevlar UD, HMCF UD, Baron UD, E Glass Fabric, Std CF Fabric, Glass UD, Kevlar Fabric	MSS UD

model training. This approach is particularly valuable when dealing with a limited dataset, as it maximizes the use of available data while providing a rigorous evaluation of the model's performance. By iteratively rotating the test material, the cross-validation process ensures that each material serves as both a training and test sample, thereby offering a comprehensive and unbiased estimate of the model's predictive accuracy. The resulting cross-validation strategy provides a robust framework for assessing the model's performance, accounting

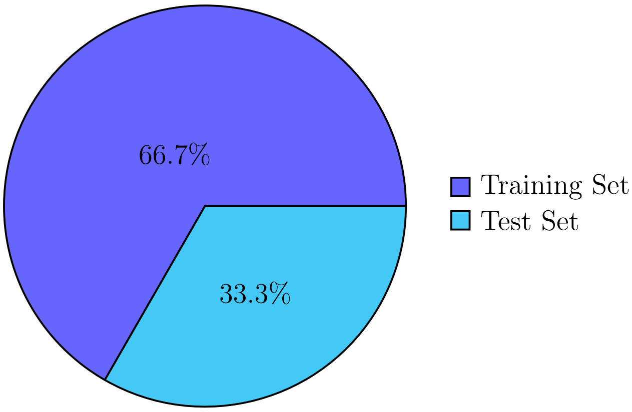

Fig. 10. Pie chart of training set and test set.

for potential variations and dependencies across different materials in the dataset. This outcome is a strong indicator that the surrogate embodies the general structure–property relations, rather than specific idiosyncrasies of the nine laminae of training, and is thus predicted to generalize to new equivalent-ply arrangements within the property envelope investigated.

The Root Mean Squared Error (RMSE) has been selected as the primary metric to evaluate the performance of the models due to its effectiveness in capturing the magnitude of prediction errors. RMSE is defined as the square root of the average squared differences between the predicted and actual values as shown in Eq. (3). This property has ensured that significant deviations from the true values are penalized more heavily, providing a clear indication of model accuracy in scenarios where outlier errors can be critical. Moreover, since RMSE is expressed in the same unit as the target variable, it has facilitated intuitive interpretation and comparison across different models.

$$\text{RMSE} = \sqrt{\frac{1}{n}\sum_{i=1}^{n}\left(y_i - \hat{y}_i\right)^2} \tag{3}$$

where:

- y_i are the observed values,
- $\hat{y}_i$ are the predicted values,
- n is the total number of observations.

3. Results and discussions

The results will be presented for both types of algorithms used, with a thorough analysis for each. For each algorithm, one scenario will include all the input variables, while another will focus exclusively on the features selected in the feature engineering section. This comparison will help evaluate the impact of feature selection on the model's performance and its predictive accuracy. Since RMSE has been selected as the reference metric, which preserves the magnitude of the variable, and given that the failure index ranges between 0 and 1, errors within a range of 10% to 15% can be considered reasonable. Furthermore, because the 1017 predicted–target pairs occupy the unit interval almost entirely along the 45° parity line, an additional scatter plot would reproduce the numeric RMSE information with little extra insight and has therefore been omitted. In addition to RMSE, other standard regression metrics such as Mean Squared Error (MSE), Mean Absolute Error (MAE), and Mean Bias Error (MBE) are also reported for the train-test split evaluation. However, for LOO cross-validation scenario, only RMSE is considered, as it has been identified as the definitive performance metric for comparative assessment.

Table 10
Performance metrics (RMSE, MSE, MAE, MBE) of the Random Forest model with Train-Test split using all features and selected features for different failure criteria.

Output variable	Metric	All features		Selected features	
		Train	Test	Train	Test
Max Stress	RMSE	0.02	0.036	0.019	0.115
	MSE	0.0004	0.001	0.0004	0.013
	MAE	0.003	0.029	0.003	0.088
	MBE	−0.00007	0.002	0.00005	−0.039
Tsai–Wu	RMSE	0.054	0.266	0.018	0.335
	MSE	0.003	0.070	0.0003	0.112
	MAE	0.007	0.171	0.002	0.282
	MBE	0.0001	0.145	−0.001	0.023
Tsai–Hill	RMSE	0.053	0.073	0.053	0.138
	MSE	0.003	0.005	0.003	0.019
	MAE	0.007	0.024	0.007	0.082
	MBE	0.0003	0.014	0.0003	−0.061
Hashin	RMSE	0.024	0.237	0.026	0.110
	MSE	0.0006	0.056	0.0007	0.012
	MAE	0.004	0.184	0.004	0.084
	MBE	−0.0001	−0.165	−0.0002	−0.082
Christensen	RMSE	0.012	0.271	0.012	0.149
	MSE	0.0001	0.073	0.0001	0.022
	MAE	0.001	0.222	0.001	0.100
	MBE	−0.0004	−0.066	−0.005	−0.063

Table 11
Performance metrics (RMSE Mean ± Std) of RF with LOO cross-validation using all features and selected features for different failure criteria.

Output variable	All features		Selected features	
	Train	Test	Train	Test
Max Stress	0.016 ± 0.001	0.147 ± 0.116	0.015 ± 0.004	0.121 ± 0.105
Tsai–Wu	0.062 ± 0.007	0.261 ± 0.196	0.028 ± 0.006	0.212 ± 0.154
Tsai–Hill	0.038 ± 0.004	0.203 ± 0.199	0.039 ± 0.004	0.224 ± 0.2326
Hashin	0.017 ± 0.002	0.076 ± 0.052	0.019 ± 0.002	0.058 ± 0.036
Christensen	0.029 ± 0.006	0.070 ± 0.070	0.027 ± 0.005	0.104 ± 0.083

3.1. Random forest

The results of the Random Forest algorithm shown in Table 10, highlights that when all features are selected, the individual results of the various failure index models, differing by the criterion used, yield lower errors, particularly for the Max Stress and Tsai–Hill criteria. Additionally, there is a smaller gap between the training and test results, which is a positive indicator of the models' generalizability. However, when averaging the results across all models, the case with the selected features produces better overall performance.

Table 11 shows the results of the LOO cross-validation for each criterion and input combination, expressed as the average RMSE obtained over 9 iterations (described in Table 9), along with the corresponding standard deviation. The results indicate that the prediction models based on the Tsai–Hill and Tsai–Wu criteria are the worst-performing, regardless of whether all features or only the selected ones are used. For example, the Tsai–Hill model with all features shows an RMSE of 0.203 and a standard deviation of 0.199 on the test data, both of which are of the same order of magnitude. On the other hand, the models that perform better in terms of generalizability, for opposite reasons, are Hashin and Christensen. Specifically, in the case with all features, the Hashin model shows an RMSE of 0.076 and a standard deviation of 0.052 on the test data. Across the nine LOO cross-validation folds, the RF surrogate preserves an RMSE ≤ 0.27 even when the excluded laminate differs by up to 150 GPa in E_{11} (Epoxy glass fabric vs. High-modulus carbon fiber ud) and 43% in density (Kevlar vs. Boron), demonstrating transferability beyond the nine training architectures.

Table 12

Performance metrics (RMSE, MSE, MAE, MBE) of the SVR model with Train-Test split using all features and selected features for different failure criteria.

Output variable	Metric	All features		Selected features	
		Train	Test	Train	Test
Max Stress	RMSE	0.042	0.112	0.102	0.184
	MSE	0.002	0.013	0.010	0.034
	MAE	0.033	0.099	0.050	0.135
	MBE	0.025	−0.072	−0.036	−0.124
Tsai–Wu	RMSE	0.007	0.051	0.023	0.128
	MSE	0.00004	0.003	0.0005	0.016
	MAE	0.006	0.036	0.008	0.118
	MBE	0.001	0.033	−0.001	0.032
Tsai–Hill	RMSE	0.007	0.130	0.182	0.252
	MSE	0.00004	0.017	0.033	0.064
	MAE	0.006	0.098	0.082	0.185
	MBE	0.001	−0.060	−0.069	−0.185
Hashin	RMSE	0.020	0.237	0.011	0.137
	MSE	0.0004	0.056	0.0001	0.019
	MAE	0.007	0.197	0.008	0.122
	MBE	−0.00004	−0.197	0.0004	−0.091
Christensen	RMSE	0.016	0.280	0.008	0.208
	MSE	0.0003	0.078	0.00006	0.043
	MAE	0.006	0.221	0.007	0.172
	MBE	−0.001	−0.069	−0.0006	−0.035

Table 13

Performance metrics (RMSE Mean ± Std) of SVR with LOO cross-validation using all features and selected features for different failure criteria.

Output variable	All features		Selected features	
	Train	Test	Train	Test
Max Stress	0.053 ± 0.009	0.208 ± 0.155	0.096 ± 0.017	0.482 ± 0.155
Tsai–Wu	0.053 ± 0.009	0.197 ± 0.182	0.028 ± 0.006	0.212 ± 0.154
Tsai–Hill	0.157 ± 0.027	0.177 ± 0.164	0.039 ± 0.004	0.224 ± 0.2326
Hashin	0.035 ± 0.006	0.132 ± 0.027	0.019 ± 0.002	0.058 ± 0.036
Christensen	0.017 ± 0.002	0.504 ± 0.496	0.027 ± 0.005	0.104 ± 0.083

3.2. Support vector regression

The results of the SVR shown in Table 12 highlight that, this time, the case with all features achieves a better average RMSE. Additionally, Max Stress, Tsai–Wu, and Tsai–Hill models individually yield better results. Conversely, for Hashin and Christensen, when considered individually, the results with the selected features are superior.

As shown in Table 13, regression models based on Max Stress, Tsai–Wu, and Tsai–Hill exhibit better performance when using all features, while models for Hashin and Christensen perform better with selected features. For example, the Christensen model reports an error of 50% with a standard deviation of 50% on the test dataset when using all features, whereas the Max Stress model reports an error of 48% with a standard deviation of 15% when using only selected features. These examples illustrate a general trend observed across most models, highlighting consistent performance differences between feature sets.

It should also be noted that the SVR results are markedly worse than those of Random Forest when evaluated against the predefined acceptance criteria for error ranges (10%–15%).

3.3. Validation strategy overview

To ensure the credibility of the numerical model and the machine-learning surrogate, a three-tiered validation procedure has been pursued. First, the FE accuracy is established through a mesh refinement study, right after mesh description in Section 2.2; convergence of peak stress and deflection to an accuracy of around ∼1% certifies the sufficiency of the discretization adopted. Second, the failure-index extraction is completely transparent and reproducible: as detailed in Section 2.3, failure indices are not coded through a UMAT but are instead obtained in post-processing by exporting the six stress components from the integration point at maximum von Mises stress and offline evaluating the indices. This approach shortcuts the parametric analyses and is consistent with certification practices of intralaminar failure by training the surrogate on the scalar maximum index, $\max(\mathrm{FI}_j)$. Third, surrogate generalizability is strictly validated: Section 2.5.4 outlines material-wise LOO cross-validation, where each laminate family is skipped in turn to ensure the model is tested on completely unseen material arrangements. Section 3 then documents the resultant performance metrics (RMSE, MAE, and standard deviation per failure criterion) on all validation folds, evidencing surrogate robustness and predictive fidelity.

3.4. Classical versus machine learning predictions

Closed–form thin–walled beam relations provide a useful first estimate of the axial–shear stress state in an orthotropic, cantilevered wing-box, yet they presuppose uniform stiffness along the span and neglect the local warping restraint introduced by rib and spar discontinuities. In the present study, however, three factors render purely closed-form prediction inadequate and motivate the ML surrogate.

First, the parameter space embraces nine markedly different orthotropic material systems and four levels of local stiffness degradation distributed over twenty-eight discrete rectangles. Classical beam theory assumes constant sectional stiffness; once orthotropy varies from case to case and transverse moduli are locally reduced by as much as eighty per-cent, the shear-flow redistribution and warping restraint deviate significantly from the analytical assumptions. Recent multiscale investigations confirm that even slender composite wing-boxes develop non-uniform shear stresses and local coupling terms that cannot be captured by closed-form Timoshenko or Euler–Bernoulli kinematics when material heterogeneity is introduced, since the such structural theories assume uniform sectional stiffness and uncoupled orthotropy; as soon as transverse moduli or fiber volume fraction vary along the span, these assumptions break down and stress prediction errors grow markedly [41–44]. Recent multiscale studies confirm that slender composite wing-boxes with blended lay-ups develop non-uniform shear flows and warping restraints that cannot be captured by single-section beam theory [45]. Therefore, the FE database used here contains stress states unreachable by classical formulas. The FE campaign therefore produces stress states that no single formula can track across the 1017 simulations.

Second, the intended application is rapid, in-service structural-health assessment. Surrogate models trained on FE data have been shown to cut response times from minutes to milliseconds while retaining FE-level fidelity, a feature essential for flight-deck decision-making and digital-twin updating [46,47]. In the present work the RF surrogate reproduces Hashin indices with an RMSE of 0.076, whereas recomputing the full FE model would require on the order of ten minutes per load case on a standard workstation; the gain therefore exceeds three orders of magnitude without forfeiting accuracy.

Third, as already pointed out in Section 2.5.3, algorithmic restraint has deliberately been exercised. Tree ensembles and kernel machines are known to dominate deeper architectures on low-sample, tabular datasets, precisely the regime characteristic of preliminary composite design. The No-Free-Lunch theorem [48] further demonstrate that, averaged over all problem classes, no learner can outperform all others [18]; adding high-capacity networks would thus enlarge the experimental matrix without an *a priori* expectation of benefit [49]. The study therefore confines itself to RF and SVR, whose bias–variance envelopes are well matched to the data and the engineering objective.

In conclusion, surrogate or hybrid ML models are increasingly preferred whenever (a) structural response must be updated in-flight or (b) parametric studies span hundreds of material or damage permutations [50–52]. Published comparisons consistently show tree ensembles, kernel machines or shallow neural surrogates outrunning and outscoring both closed-form and reduced FEM solvers on tabular composite datasets of similar size [53]. Therefore, although analytical and numerical models remains a valuable physics-based cross-check, they cannot replace the data-driven surrogate when material heterogeneity and/or local property variations are present.

4. Conclusions and future perspectives

This paper demonstrates a machine learning model that predicts the structural health of a wing box simulated with nine composite materials. It shows the model's capability to capture complex relationships between material properties and structural health, essential for safe aircraft operation. Limitations and future directions are also discussed.

A machine learning model is developed using a comprehensive dataset of composite material properties under fixed geometry and boundary conditions. FE analyses provided data for both training and testing, capturing the intricate link between material behavior and wing box health condition. The present surrogate is certified for equivalent-ply materials whose mechanical properties remain within the ranges spanned in Table 2; outside this convex hull, the model must be re-trained or enriched with higher-fidelity data.

Although promising, the results indicate that further refinement in dataset variability is needed to enhance predictive accuracy. The foremost challenges include the control of the complexity of the models to avoid over-fitting, and the improvement of the training data quantity and quality. Future research will investigate other architectures, optimization techniques, and the integration of real-world experimental data (e.g., to address delamination and non-linearity). Future research may further emphasize quantifying the uncertainty in the predictions to guarantee the model's generalizability under real-world aircraft maintenance.

CRediT authorship contribution statement

Dario Magliacano: Writing – review & editing, Writing – original draft, Supervision, Software, Project administration, Methodology, Investigation, Formal analysis, Data curation, Conceptualization. **Vincenza Tufano:** Writing – original draft, Validation, Methodology, Investigation, Formal analysis, Data curation. **Annalisa Letizia:** Supervision, Methodology, Formal analysis, Data curation, Conceptualization. **Bernardo Sessa:** Visualization, Validation, Supervision, Software, Resources, Funding acquisition. **Matteo Filippi:** Visualization, Supervision, Software, Resources, Project administration, Funding acquisition.

Declaration of competing interest

The authors declare that they have no known competing financial interests or personal relationships that could have appeared to influence the work reported in this paper.

Acknowledgments

The authors acknowledge the support of the Italian Ministry of University and Research (MUR) and the Sustainable Mobility Center (MOST), Italy through the project PNRR - M4C2 - CNMS - Spoke 1, funded under the scheme CN00000023 - PNRR – M4C2 Inv. 1.4 with grant agreement no. 55-PRR22-1155-22-GG002138.

Data availability

No data was used for the research described in the article.

References

[1] Spencer BF, Sim S, Kim RE, Yoon H. Advances in artificial intelligence for structural health monitoring: A comprehensive review. KSCE J Civ Eng 2025;29(3):100203. http://dx.doi.org/10.1016/j.kscej.2025.100203.

[2] Numan M. Advancements in structural health monitoring: A review of machine learning approaches for damage detection and assessment. Int J Comput Civ Struct Eng 2024;20(1):124–42. http://dx.doi.org/10.22337/2587-9618-2024-20-1-124-142.

[3] Aydın Y, Cakiroglu C, Bekdaş G, Geem ZW. Fatigue predictive modeling of composite materials for wind turbine blades using explainable gradient boosting models. Coatings 2025;15(3):325. http://dx.doi.org/10.3390/coatings15030325.

[4] Tosti Balducci G, Chen B, Möller M, Gerritsma M, De Breuker R. Predicting open-hole laminates failure using support vector machines with classical and quantum kernels. 2024, ArXiv, arXiv:2405.02903.

[5] Azad MM, Kim HS. Hybrid deep convolutional networks for the autonomous damage diagnosis of laminated composite structures. Compos Struct 2024;329. http://dx.doi.org/10.1016/j.compstruct.2023.117792.

[6] Karuppusamy M, Thirumalaisamy R, Palanisamy S, Nagamalai S, Massoud EES, Ayrilmis N. A review of machine learning applications in polymer composites: Advancements, challenges, and future prospects. J Mater Chem A 2025;13:16290–308. http://dx.doi.org/10.1039/D5TA00982K.

[7] Shafighfard T, Demir E, Yildiz M. Design of fiber-reinforced variable-stiffness composites for different open-hole geometries with fiber continuity and curvature constraints. Compos Struct 2019;226:111280. http://dx.doi.org/10.1016/j.compstruct.2019.111280.

[8] Shafighfard T, Mieloszyk M. Experimental and numerical study of the additively manufactured carbon fibre reinforced polymers including fibre bragg grating sensors. Compos Struct 2022;299:116027. http://dx.doi.org/10.1016/j.compstruct.2022.116027.

[9] El Hajj Chehade F, Younes R. Structural reliability software and calculation tools: a review. Innov Infrastruct Solutions 2020;5(1). http://dx.doi.org/10.1007/s41062-020-0282-4.

[10] Fanteria D, Panettieri E. A non-linear model for in-plane shear damage and failure of composite laminates. Aerotec Missili Spaz 2014;93:17–24. http://dx.doi.org/10.1007/BF03404672.

[11] Filippi M, Magliacano D, Petrolo M, Carrera E. Variable-kinematics finite elements for propagation analyses of two-dimensional waveguides. In: 30th AIAA/cEAS aeroacoustics conference, 2024. 2024, http://dx.doi.org/10.2514/6.2024-3078.

[12] Filippi M, Magliacano D, Petrolo M, Carrera E. Wave propagation in pre-stressed structures with geometric non-linearities through carrera unified formulation. In: 30th AIAA/cEAS aeroacoustics conference, 2024. 2024, http://dx.doi.org/10.2514/6.2024-3028.

[13] Filippi M, Magliacano D, Petrolo M, Carrera E. Wave propagation in prestressed structures with geometric nonlinearities through carrera unified formulation. AIAA J 2025;63(1):292–308. http://dx.doi.org/10.2514/1.J064695.

[14] Teng Z. Thermo-based fatigue life prediction: A review. Fatigue Fract Eng Mater Struct 2023;46(9):3121–44. http://dx.doi.org/10.1111/ffe.14079.

[15] Ma Q, Feng Z, Ma H, An Z, Zeng S, Bai X. Research on residual life prediction method of composites based on equivalent number of cycles conversion. J Fail Anal Prev 2024;24(2):708–20. http://dx.doi.org/10.1007/s11668-024-01875-0.

[16] Kong BO, Kim MS, Kim BH, Lee JH. Prediction of creep life using an explainable artificial intelligence technique and alloy design based on the genetic algorithm in creep-strength-enhanced ferritic 9% Cr steel. Met Mater Int 2023;29(5):1334–45. http://dx.doi.org/10.1007/s12540-022-01312-7.

[17] Ribeiro Junior RF, Gomes GF. On the use of machine learning for damage assessment in composite structures: A review. Appl Compos Mater 2024;31(1):1–37. http://dx.doi.org/10.1007/s10443-023-10161-5.

[18] Dadras Eslamlou A, Huang S. Artificial-neural-network-based surrogate models for structural health monitoring of civil structures: A literature review. Buildings 2022;12(12). http://dx.doi.org/10.3390/buildings12122067.

[19] Altabey WA, Noori M. Artificial-intelligence-based methods for structural health monitoring. Appl Sci 2022;12(24). http://dx.doi.org/10.3390/app122412726.

[20] Jia J, Li Y. Deep learning for structural health monitoring: Data, algorithms, applications, challenges, and trends. Sensors 2023;23(21). http://dx.doi.org/10.3390/s23218824.

[21] Nguyen-Tran H, Bui-Tien T, Wahab M, Bui-Ngoc D. Damage detection in structural health monitoring using combination of deep neural networks. J Mater Eng Struct 2020;7(4).

[22] Chang CM, Tzu-Kang L, Chang CW. Applications of neural network models for structural health monitoring based on derived modal properties. Meas: J Int Meas Confed 2018;129:457–70. http://dx.doi.org/10.1016/j.measurement.2018.07.051.

[23] Kekez S, Kubica J. Connecting concrete technology and machine learning: proposal for application of ANNs and CNT/concrete composites in structural health monitoring. RSC Adv 2020;10(39):23038–48. http://dx.doi.org/10.1039/D0RA03450A.

[24] Alaimo A, Barracco A, Milazzo A, Orlando C. Structural health monitoring procedure for composite structures through the use of artificial neural networks. Aerotec Missili Spaz 2015;94:14–22. http://dx.doi.org/10.1007/BF03404684.

[25] Casaburo A, Magliacano D, Petrone G, Franco F, De Rosa S. Optimizing the acoustic properties of a meta-material using machine learning techniques. In: Proceedings of INTER-nOISE 2021 - 2021 international congress and exposition of noise control engineering. 2021, http://dx.doi.org/10.3397/IN2021-2294.

[26] Wang Q, Qin H, Jia L, Li Z, Zhang G, Li Y, Liu Y. Failure prediction and optimization for composite pressure vessel combining FEM simulation and machine learning approach. Compos Struct 2024;337. http://dx.doi.org/10.1016/j.compstruct.2024.118099.

[27] Nakka R, Harursampath D, Ponnusami SA. A generalised deep learning-based surrogate model for homogenisation utilising material property encoding and physics-based bounds. Sci Rep 2023;13(1). http://dx.doi.org/10.1038/s41598-023-34823-3.

[28] Corporation H. T700S standard modulus carbon fiber - technical data sheet. 2025, URL https://www.rockwestcomposites.com/on/demandware.static/Sites-RWC-Site/Sites-rwc-master-catalog/-/downloads/T700SDataSheet.pdf.

[29] Toray Carbon Fibers America I. M55j high modulus carbon fiber - technical data sheet. 2025, URL https://www.rockwestcomposites.com/on/demandware.static/-/Sites-rwc-master-catalog/default/dw46b18669/downloads/M55J.pdf.

[30] DuPont. Kevlar® 49 aramid fiber - technical guide. 2020, URL https://www.dupont.com/content/dam/dupont/amer/us/en/safety/public/documents/en/Kevlar_Technical_Guide_0319.pdf.

[31] AZoM. Properties of E-glass fibre. 2023, URL https://www.azom.com/properties.aspx?ArticleID=764.

[32] Inc. SM. Boron fiber properties. 2024, URL https://www.specmaterials.com/boron-fiber-test-page.

[33] Brothers G. Comparison of WEST system® epoxy physical properties. 2024, URL https://eu.westsystem.com/compare-epoxy-physical-properties/.

[34] Seresta O, Gürdal Z, Adams DB, Watson LT. Optimal design of composite wing structures with blended laminates. Compos Part B: Eng 2007;38(4):469–80. http://dx.doi.org/10.1016/j.compositesb.2006.08.005.

[35] Evgeniou T, Pontil M. Support vector machines: Theory and applications. In: Machine learning and its applications: advanced lectures. Springer Berlin Heidelberg; 2001, p. 249–57. http://dx.doi.org/10.1007/3-540-44673-7_12.

[36] Breiman L. Random forests. Mach Learn 2001;45(1):5–32. http://dx.doi.org/10.1023/A:1010933404324.

[37] Bagherzadeh F, Shafighfard T, Khan RMA, Szczuko P, Mieloszyk M. Prediction of maximum tensile stress in plain-weave composite laminates with interacting holes via stacked machine learning algorithms: A comparative study. Mech Syst Signal Process 2023;195:110315. http://dx.doi.org/10.1016/j.ymssp.2023.110315.

[38] Shafighfard T, Kazemi F, Bagherzadeh F, Mieloszyk M, Yoo DY. Chained machine-learning model for predicting load capacity and ductility of steel fibre–reinforced concrete beams. Comput-Aided Civ Infrastruct Eng 2024;39:3573–94. http://dx.doi.org/10.1111/mice.13164.

[39] Borisov V, Leemann T, Seßler K, Haug J, Vogt S, Ling C, Rawat B, Trimpe S, Lucic M, Hofer C. Deep neural networks and tabular data: A survey. 2022, ArXiv, arXiv:2110.01889.

[40] Grinsztajn L, Oyallon E, Varoquaux G. Why do tree-based models still outperform deep learning on tabular data?. 2023, ArXiv, arXiv:2207.08815.

[41] Chakravarty UK. On the modeling of composite beam cross-sections. Compos Part B: Eng 2011;42(4):982–91. http://dx.doi.org/10.1016/j.compositesb.2010.10.012.

[42] Doeva O, Masjedi PK, Weaver PM. Static deflection of fully coupled composite timoshenko beams: An exact analytical solution. Eur J Mech A Solids 2020;81:103975. http://dx.doi.org/10.1016/j.euromechsol.2020.103975.

[43] Rashidinejad E, Ahmadi H, Hajikazemi M, Van Paepegem W. Closed-form analytical solutions for predicting stress transfers and thermo-elastic properties of short fiber composites. Mech Adv Mater Struct 2022;30:1–21. http://dx.doi.org/10.1080/15376494.2022.2104973.

[44] Miranda M, Li R, Iorga L, Pinho ST. Multiscale modelling strategy for a novel wingbox structure with increased bend-twist coupling. Compos Struct 2025;370:119291. http://dx.doi.org/10.1016/j.compstruct.2025.119291.

[45] Makkar G, Smith C, Drakoulas G, Kopsaftopoulos F, Gandhi F. A machine learning framework for physics-based multi-fidelity modeling and health monitoring for a composite wing. In: ASME 2022 international mechanical engineering congress and exposition. 2023, http://dx.doi.org/10.1115/IMECE2022-94850.

[46] Mainini L, Willcox K. Surrogate modeling approach to support real-time structural assessment and decision making. AIAA J 2015;53(6):1612–26. http://dx.doi.org/10.2514/1.J053464.

[47] Torzoni M, Manzoni A, Mariani S. A multi-fidelity surrogate model for structural health monitoring exploiting model order reduction and artificial neural networks. Mech Syst Signal Process 2023;197:110376. http://dx.doi.org/10.1016/j.ymssp.2023.110376.

[48] Goldblum M, Finzi M, Rowan K, Wilson AG. The no free lunch theorem, Kolmogorov complexity, and the role of inductive biases in machine learning. 2024, ArXiv, arXiv:2304.05366.

[49] Sorour SS, Saleh CA, Shazly M. A review on machine learning implementation for predicting and optimizing the mechanical behaviour of laminated fiber-reinforced polymer composites. Heliyon 2024;10(13):e33681. http://dx.doi.org/10.1016/j.heliyon.2024.e33681.

[50] Liang L, Liu M, Martin C, Sun W. A deep learning approach to estimate stress distribution: a fast and accurate surrogate of finite-element analysis. J R Soc Interface 2018;15(138):20170844. http://dx.doi.org/10.1098/rsif.2017.0844.

[51] Etim B, Al-Ghosoun A, Renno J, Seaid M, Mohamed MS. Machine learning-based modeling for structural engineering: A comprehensive survey and applications overview. Buildings 2024;14(11). http://dx.doi.org/10.3390/buildings14113515.

[52] Cha Y-J, Ali R, Lewis J, Büyüköztürk O. Deep learning-based structural health monitoring. Autom Constr 2024;161:105328. http://dx.doi.org/10.1016/j.autcon.2024.105328.

[53] Badarinath P, Chierichetti M, Davoudi Kakhki F. A machine learning approach as a surrogate for a finite element analysis: Status of research and application to one dimensional systems. Sensors 2021;21:1654. http://dx.doi.org/10.3390/s21051654.